

## Review

## Metal-organic framework nanosheets: Preparation and applications

Yan-zhou Li<sup>a,b,1</sup>, Zhi-hua Fu<sup>a,1</sup>, Gang Xu<sup>a,\*</sup><sup>a</sup> State Key Laboratory of Structural Chemistry, Fujian Institute of Research on the Structure of Matter, Chinese Academy of Sciences (CAS) 155 Yangqiao Road West, Fuzhou, Fujian 350002, PR China<sup>b</sup> University of Chinese Academy of Sciences, Chinese Academy of Sciences, 100039 Beijing, PR China

## ARTICLE INFO

## Article history:

Received 16 July 2018

Accepted 25 February 2019

Available online 6 March 2019

## Keywords:

Metal-organic framework

Nanosheet

Top-down

Bottom-up

Application

## ABSTRACT

Metal-organic framework (MOF) nanosheets have attracted extensive attention due to their remarkable properties, such as nanoscale and tunable thickness, adjustable structure and function, high-aspect-ratio, large surface area, more exposed accessible active site, favorable mechanical flexibility, and optical transparency. This article aims to review the latest developments in MOF nanosheets. Firstly, the assortments of the synthetic methods of MOF nanosheets will be introduced. Then, the wide applications and utilization of these ultrathin MOF nanosheets in the fields of electronics, gas separation, catalysis, sensors, energy storage/transfer, and as enzyme inhibitors will also be explored. Finally, the prospects and challenges of MOF nanosheets will be presented.

© 2019 Elsevier B.V. All rights reserved.

## Contents

|   |    |
|---|----|
| 1. Introduction   | 80 |
| 2. Synthesis strategies of MOF nanosheets                         | 80 |
| 2.1. Top-down methods   | 81 |
| 2.1.1. Micromechanical exfoliation                                | 81 |
| 2.1.2. Sonication-assisted liquid exfoliation                     | 81 |
| 2.1.3. Solvent-induced delamination exfoliation                   | 88 |
| 2.1.4. Exotic substance intercalation-assisted liquid exfoliation | 88 |
| 2.2. Bottom-up methods  | 88 |
| 2.2.1. Hydro-solvothermal syntheses                               | 88 |
| 2.2.2. Interface-mediated syntheses                               | 89 |
| 2.2.3. Langmuir-Blodgett (LB) method                              | 90 |
| 3. Applications of MOF nanosheets                                 | 92 |
| 3.1. Separation   | 92 |
| 3.1.1. Gas separation   | 92 |
| 3.1.2. Nanofiltration   | 94 |

**Abbreviations:** MOF, metal-organic framework; TMD, transition metal dichalcogenides; LB, Langmuir-Blodgett; acac<sub>2</sub>-trien, di(acetylacetonate)-triethylene tetramine; An, 2,5-dihydroxy-1,4-benzoquinone dianion; AFM, atomic force microscopy; IN, isonicotinate; pymS<sub>2</sub>, dipyrimidindisulfide; Gly-Thr, dipeptide glycylthreonine; DMF, dimethylformamide; THF, tetrahydrofuran; 2,3-DMS, 2,3-dimethylsuccinate; DMS, 2,2'-dimethylsuccinate; PW, paddle wheel; TDA, S(CH<sub>2</sub>COO)<sub>2</sub><sup>2-</sup>; Ln, lanthanide; SAED, selected area electron diffraction; DPDS, 4,4'-dipyridyl disulfide; H<sub>2</sub>TCPP, 5,10,15,20-tetrakis(4-carboxyphenyl)porphyrin; TEM, transmission electron microscopy; BHT, benzenehexathiol; HDMS, 1,1,1,3,3,3-hexamethyldisilazane; BDCA, 1,4-benzenedi carboxylic acid; LBL, layer-by-layer; tpy, terpyridine; THT, 1,2,5,6,9,10-triphenylenehexathiol; OER, oxygen evolution reaction; HER, hydrogen evolution reaction; bim, benzimidazole; BET, Brunauer-Emmett-Teller; GPUs, gas permeation units; MMMs, mixed-matrix membranes; TOF, turnover frequency; TPY, 4'-(4-benzoate)-(2,2',2''-terpyridine)-5,5''-dicarboxylate; NAHN, nanosheet-assembled hollow nanocube; TMB, 3,3',5,5'-tetramethylbenzidine; dsDNA, double-stranded DNA; ssDNA, single-stranded DNA; TAMRA, tetramethylrhodamine; FAM, fluorescein; H<sub>2</sub>DOBDC, 2,5-dihydroxyterephthalic acid; ABSHD, alkaline battery-supercapacitor hybrid devices; CNTs, carbon nanotubes; bpy, 4,4'-bipyridine; Otf, trifluoromethanesulfonate.

\* Corresponding author.

E-mail address: [gxu@fjirsm.ac.cn](mailto:gxu@fjirsm.ac.cn) (G. Xu).<sup>1</sup> These authors contributed equally to this work.

|  |     |
|--|-----|
| 3.2. Catalysts . . . . .                   | 94  |
| 3.2.1. Electrocatalysis . . . . .          | 94  |
| 3.2.2. Organic reaction . . . . .          | 97  |
| 3.3. Sensing . . . . .                     | 100 |
| 3.3.1. Biosensing . . . . .                | 100 |
| 3.3.2. Optochemical sensor . . . . .       | 100 |
| 3.3.3. Electrochemical sensing . . . . .   | 100 |
| 3.4. Energy storage and transfer . . . . . | 101 |
| 3.5. Enzyme inhibitor . . . . .            | 102 |
| 4. Conclusion and prospects . . . . .      | 103 |
| Acknowledgements . . . . .                 | 105 |
| References . . . . .                       | 105 |

## 1. Introduction

Recently, to scale-down the metal-organic frameworks (MOFs) into nanoregime has become a worthwhile goal and provided new insights into MOF-based studies/applications [1–10]. Nanostructured MOFs, as a fascinating kind of crystalline material, also constructed by the diversified interconnection of the organic linkers and metal nodes. Recently, MOF nanosheets have attracted great attention due to their distinctive characteristics such as nanoscale and tunable thickness, high-aspect-ratio, large surface area, more exposed accessible active site, favorable mechanical flexibility, and optical transparency [11–111]. These features endow MOF nanosheets with enhanced applications in gas separation, catalysts, sensing, energy storage and transfer, and enzyme inhibitor [23,28,36–45,84–85,112–130].

Until now, MOF nanosheets have been extensively prepared with two main methods: top-down delamination and bottom-up syntheses. Top-down method is a powerful approach to make the disintegration of the bulk materials to delaminated nanosheets. However, the parent MOF materials normally should have the following requirements: 1) they should be layered crystal structures with weak interaction between layers (such as van der Waals forces, hydrogen bonding and so on) [12–27]; 2) the 2D structures should possess strong mechanical and chemical stability, which can bear the external force (sonication, shaking and mechanical force) and chemicals (Li-intercalation, solvent intercalation) to produce nanosheets instead of to be broken down or destroyed into nanoparticles [28,29,69,71]. Comparatively, relative less MOF nanosheets were synthesized by using the bottom-up method. Notably, some MOFs with 3D crystal structure can be successfully synthesized into nanosheet with this method [41,45,123,128]. In order to build up the relationship between the parent MOF structure and the preparation methods of the MOF nanosheets, we have screened almost all the reported MOFs in this paper. The interlayer distances are statistically listed to roughly explain what would make a specific MOF to be top-down exfoliated or directly bottom-up synthesized. From the results in Fig. 1 and Table 1, it is found that the preparation methods have weak relationship with the interlayer distances. However, it can be found that the top-down method has larger proportion than the bottom-up method for the preparation of MOF nanosheets till now (Fig. 1).

On the other hand, the successful preparation and structural features originating from sheet-like morphology of the MOF nanosheets inspired the research about their applications. For example, ultra-thin thickness and larger lateral area of MOF nanosheets can provide enough flexibility for the fabrication of membrane separator. And the regular nano/micro-pores, ultrathin in thickness and high crystallinity in MOF nanosheets can efficiently promote the molecular selectivity in size as well as enhance the permeation of gas/liquid molecules [23,37–38]. Moreover, the exposed well-defined active site density of MOF nanosheets

increases the probability of contact of guest molecules and improves the catalysis efficiency while promoting the reaction rate [39]. In addition, the large accessible surface area, ultrathin thickness and intrinsic biodegradability of MOF nanosheets are beneficial to the substrate diffusion and the release of the product, rendering improved performance in the electrochemical reactions [40,41], and sensing [28,42]. Furthermore, the high loading capacity of MOF nanosheets is beneficial to energy storage and conversion [43–45].

This manuscript aims to elaborate the advancements of MOF nanosheets until 2018. For instance, in 2016, Zamora wrote a feature article on cooking 2D polymers [46] with few MOF nanosheets. Moreover, Jin conducted a mini-review of 2D materials and introduced two examples of 2D MOFs as the separation membranes [47]. In 2017, Nishihara had described several MOF nanosheets [48]. In addition, Zhang had reviewed MOF nanosheets by focusing on their syntheses [49,50]. Over the past years, many new MOF nanomaterials have been developed and their corresponding properties have also been explored. The results have highlighted various novel MOF nanosheets, but few related studies are available. Certainly, a review summarizing the newly developed MOF nanosheets for different applications has great implications for the subsequent development of MOF-derived materials. Hopefully, this review will help researchers to obtain particular insights into MOF nanosheets and establish new strategies for designing and preparing MOF nanosheets for high-performance applications.

Herein, the recent advances in MOF nanosheets with regard to their preparation and potential applications will be elaborated comprehensively. Typically, the porous nanosheet materials (transition metal oxides or thin carbon materials) fabricated using MOF nanosheets will be excluded from this study [51]. In this article, the general information about the preparation strategies of MOF nanosheets will be introduced. Secondly, representative examples of MOF nanosheets will be summarized in section two in terms of their functions and applications. Finally, the challenges and opportunities of MOF nanomaterials will be discussed in section three.

## 2. Synthesis strategies of MOF nanosheets

Specifically, the synthesis of nanoscale MOFs has become a research hotspot [52–54], particularly, the preparation of nanoscale MOFs with nanosheet morphology has caught wide attention from scientists. Reliable production of the atomically thin MOF nanosheets with specific properties is essential not only for translating their various applications [55–57], but also for fulfilling the specific requirements that the bulk MOFs cannot accomplish in applications. Importantly, the potential performances and applications of MOFs may also accelerate the discovery of synthesis

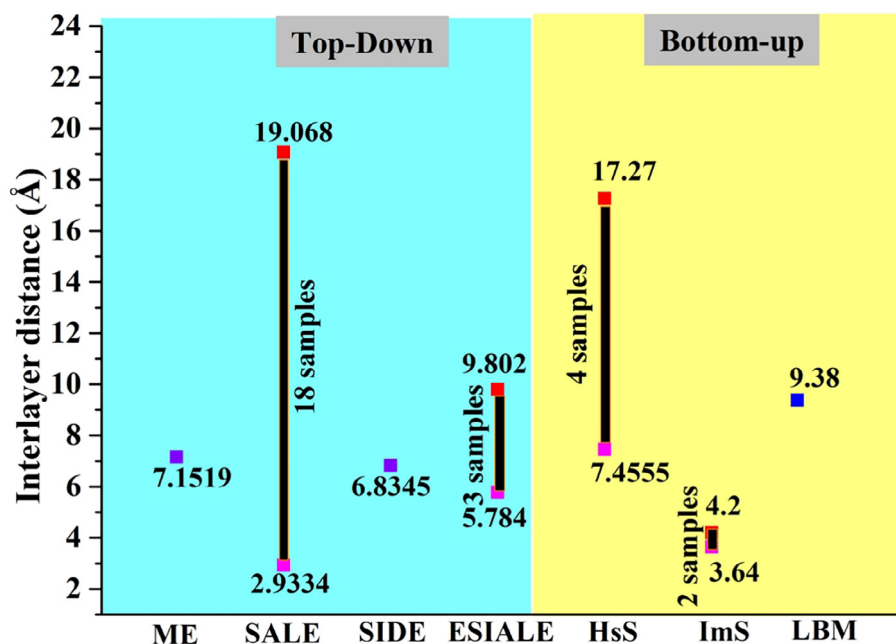


**Fig. 1.** The preparation methods of MOF nanosheets vs the interlayer distances of their corresponding structures. (ME: Micro-mechanical exfoliation; SALE: Sonication-assisted liquid exfoliation; SIDE: Solvent-induced delamination exfoliation; ESIALE: Exotic substance intercalation-assisted liquid exfoliation; HsS: Hydro-solvothermal syntheses; ImS: Interface-mediated syntheses; LBM: Langmuir-Blodgett (LB) method.)

method for MOF nanosheets. Here, the available methods for preparing MOF nanosheets have been reviewed in this section. Firstly, we will focus on the top-down methods, including micromechanical exfoliation (ME), sonication-assisted liquid exfoliation (SALE), solvent-induced delamination exfoliation (SIDE), and exotic substance intercalation-assisted liquid exfoliation (ESIALE). Later, the bottom-up approaches will also be presented, including hydro-solvothermal synthesis (HsS), interface-mediated synthesis (ImS), and Langmuir-Blodgett (LB) method (LBM), which are more versatile in principle and can produce tailorable MOF nanosheets.

## 2.1. Top-down methods

### 2.1.1. Micromechanical exfoliation

Graphene has been exfoliated and identified in 2004 by micromechanical cleavage using adhesive tape. Since then, the preparation of atomically thin flakes has become a meaningful breakthrough and historic jump in this evolution research field. Results of material science research suggest that almost all atomically thin flakes of 2D inorganic layered materials can be peeled from their parent bulk crystals [1,52,58–60]. In this delamination process, the mechanical force from human hands is employed to peel the bulk layered materials into ultrathin nanosheets with single or few layers. Typically, the success of such approach should be attributed to the strong covalent bonds in the 2D layered structure formed in the layered bulk materials, together with weak van der Waals bonds, hydrogen bond, or ionic interactions between layers.

Micromechanical exfoliation has been frequently used to fabricate atomically thin layers of graphene and TMDs, but it is rarely used to synthesize MOF materials with layered structures. In 2015, Clemente-León, Coronado, and co-workers had first successfully cleaved the ultrathin nanosheets from the bulk 2D MOFs  $[M^{III}(\text{acac}_2\text{-trien})][Mn^{II}Cr^{III}(X_2An)_3]$  ( $M = \text{Fe, Ga}$ ;  $X = \text{Cl, Br}$ ) using micromechanical exfoliation [61]. As shown in Fig. 2a and b, the compounds are comprised of the anionic 2D honeycomb structural unilateral-based layers  $[Mn^{II}Cr^{III}(Cl_2An)_3]^-$ , and such configuration has rendered decreased interlayer separation (Fig. 2c).

To date, various atomically thin nanosheets have been efficiently produced using micro-mechanical cleavage. In a typical mechanical exfoliation process, the bulk layered materials are first of all attached onto the tape before another adhesive tape is crossed to peel, and the tape is peeled finally. The ultrathin flakes can be obtained by repeating this process several times. The ultrathin 2D materials will be transferred on the substrate by removing the tape, when they are attached onto the silicon wafer or other clean surfaces. Lastly, the good-quality MOF nanosheets about 2 nm in thickness with micrometer lateral dimension can be obtained. These thin flakes can be identified clearly on the optical images by the color contrast difference between the substrate and nanosheets (Fig. 2d). However, the thickness of nanosheets on AFM topography is highly dispersed (Fig. 2e). In addition, the same method can also be extrapolated to an analogous ionic layered compound  $[Fe^{III}(\text{sal}_2\text{-trien})][Mn^{II}Cr^{III}(Cl_2An)_3]$ . In particular, large flakes can be isolated with the well-defined terraces 2 nm in thickness, which may be consistent with the thickness of single layers in the crystal structure (Fig. 2f).

To sum up, micromechanical exfoliation is a conventional method to fabricate high-quality thin MOF nanosheets, especially the single-layer nanosheets, which can serve as a non-chemical destructive technique. Typically, neither chemical reactions nor other chemicals are used during the preparation. Therefore, the clean nanosheets with atomic thickness but no chemical influence can be used to study their unique properties, which are distinct from their bulk materials.

### 2.1.2. Sonication-assisted liquid exfoliation

2D nanosheets can also be obtained using other mechanical forces. For instance, Coleman et al. had exfoliated the layered bulk graphite and TMDs into ultrathin nanosheets with large quantities in liquid assisted by sonication [62–64]. Thereafter, the sonication-assisted liquid exfoliation method has been largely developed to fabricate a number of inorganic layered bulk materials [65–68] as well as 2D MOFs [12,13–27].

Early in 2010, Zamora had synthesized a 2D MOF  $[Cu_2Br(IN)_2]_n$  constructed by the  $[Cu_2Br(IN)]_4$  squares (Fig. 3a) [13]. Specifically,

**Table 1**  
Preparation methods and structures of the parent materials of MOF nanosheets.

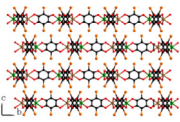
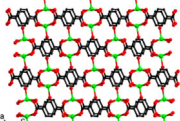
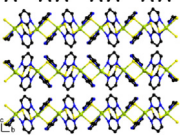
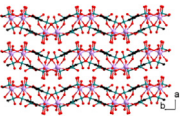
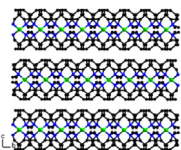
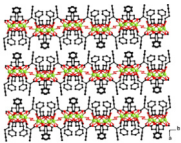
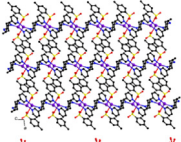
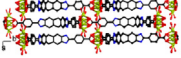
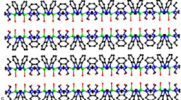
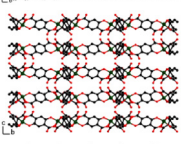
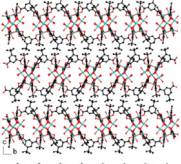
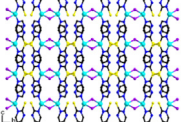
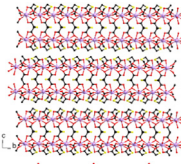
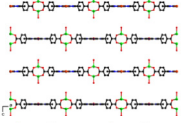
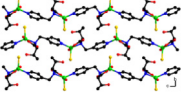
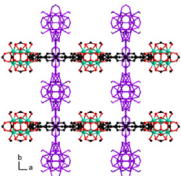
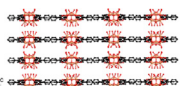
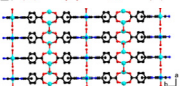
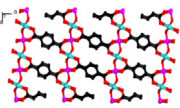
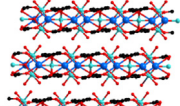
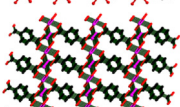
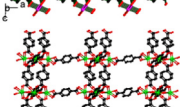
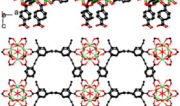
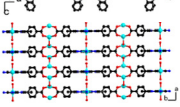
| Preparation method |      | Formular  | Crystal structure   | Space group                    | Interlayer distance (Å) | Ref  |
|--------------------|------|---|---|--------------------------------|-------------------------|------|
| Top down methods   | ME   | $[\text{Mn}^{\text{II}}\text{Cr}^{\text{III}}(\text{Br}_2\text{An})_3]$   |    | $C2/c$ (15)-monoclinic         | 7.1519                  | [61] |
|                    | SALE | $\{\text{Zn}_2(\text{TPA})_4(\text{H}_2\text{O})_{22}\}_n$  |    | $P2_1/c$ (14)-monoclinic       | 2.9334                  | [12] |
|                    |      | $[\text{Cu}_2\text{Br}(\text{IN})_2]_n$   |    | $Pbcn$ (60)-orthorhombic       | 3.3576                  | [13] |
|                    |      | $[\text{Cu}(\mu\text{-pym}_2\text{S}_2)(\mu\text{-Cl})_n]$  |    | $C2/m$ (12)-monoclinic         | 6.8345                  | [14] |
|                    |      | $[\text{Zn}(\text{Gly-Ala})_2]$   |    | $P2_12_12_1$ (19)-orthorhombic | 5.7697                  | [15] |
|                    |      | $[\text{Cu}(\text{bpy})_2(\text{OTf})_2]$   |   | $Pna2_1$ (33)-orthorhombic     | 7.1760                  | [16] |
|                    |      | $\text{Mn}(\text{C}_6\text{H}_8\text{O}_4)(\text{H}_2\text{O})$   |  | $Pbca$ (61)-orthorhombic       | 15.6453                 | [17] |
|                    |      | $[\text{Fe}(\text{Py}_2\text{th})_2]_n$   |  | $Pbca$ (61)-orthorhombic       | 7.9973                  | [18] |
|                    |      | $[\text{Co}(\text{C}_6\text{H}_8\text{O}_4)(\text{H}_2\text{O})]$   |  | $Cmca$ (64)-orthorhombic       | 10.9588                 | [19] |
|                    |      | $\text{Mn}_3(2,3\text{-DMS})_3(\text{H}_2\text{O})_2$   |  | $P2_1/c$ (14)-monoclinic       | 11.2310                 | [20] |
|                    |      | $\text{Zn}(\text{bmp-bdc})(\text{DMF})$   |  | $P\bar{1}$ (2)-triclinic       | 9.4000                  | [21] |
|                    |      | $\text{Ln}[(\text{HO}_3\text{P})_2\text{CH}-\text{C}_6\text{H}_4-\text{CH}(\text{PO}_3\text{H})(\text{PO}_3\text{H}_2)]\cdot 4\text{H}_2\text{O}$ |  | $P2_1/c$ (14)-monoclinic       | 8.5500                  | [22] |

Table 1 (continued)

| Preparation method | Formular   | Crystal structure   | Space group   | Interlayer distance (Å)                 | Ref    |      |
|--------------------|--|---|---|---|--------|------|
|                    | Zn <sub>2</sub> (bim) <sub>4</sub>   |    | C2/c (15)-monoclinic  | 9.7555                                  | [23]   |      |
|                    | [Ln <sub>2</sub> (C <sub>10</sub> H <sub>8</sub> O <sub>4</sub> ) <sub>3</sub> (H <sub>2</sub> O)]   |    | P2 <sub>1</sub> /c (14)-monoclinic  | 15.3688                                 | [24]   |      |
|                    | {[Ag(N,N'-((1 <i>r</i> ,4 <i>r</i> )-cyclohexane-1,4-diyl)bis(1-(pyridin-3-yl)methanimine))-(MeCN)](CF <sub>3</sub> SO <sub>3</sub> ) <sub>n</sub> } |    | P2 <sub>1</sub> /c (14)-monoclinic  | 11.4447                                 | [25]   |      |
|                    | Cd-TPA   |    | C2/c (15)-monoclinic  | 4.6917                                  | [26]   |      |
|                    | Zn <sub>2</sub> (Bim) <sub>3</sub>   |    | C2/m (12)-monoclinic  | 16.583                                  | [37]   |      |
|                    | Ti <sub>2</sub> (HDOBDC) <sub>2</sub> (H <sub>2</sub> DOBDC)   |   | P3̄1c (1 6 3)-trigonal  | 5.8490                                  | [42]   |      |
|                    | Ni <sub>8</sub> (5-bbdc) <sub>6</sub> (μ-OH) <sub>4</sub>  |  | P2 <sub>1</sub> /c (14)-monoclinic  | 19.0680                                 | [114]  |      |
| SIDE               | [Cu(μ-pym <sub>2</sub> S <sub>2</sub> )(μ-Cl)] <sub>n</sub>  |  | C2/m (12)-monoclinic  | 6.8345                                  | [69]   |      |
| ESIALE             | [La <sub>2</sub> (TDA) <sub>3</sub> ]·2H <sub>2</sub> O  |  | Pbcn (60)-orthorhombic  | 7.9083                                  | [28]   |      |
|                    | Zn <sub>2</sub> (PdTCPP)   |  | I4/m (87)-tetragonal  | 9.8020                                  | [29]   |      |
|                    | [Zn(l( <i>d</i> )-Py-Thr)(H <sub>2</sub> O)(Cl)]   |  | P2 <sub>1</sub> 2 <sub>1</sub> 2 <sub>1</sub> (19)-orthorhombic                     | 5.7840                                  | [71]   |      |
| Bottom up methods  | HsS  | ST-ZrBTB  |  | I4 <sub>1</sub> /amd (1 4 1)-tetragonal | 10.000 | [80] |

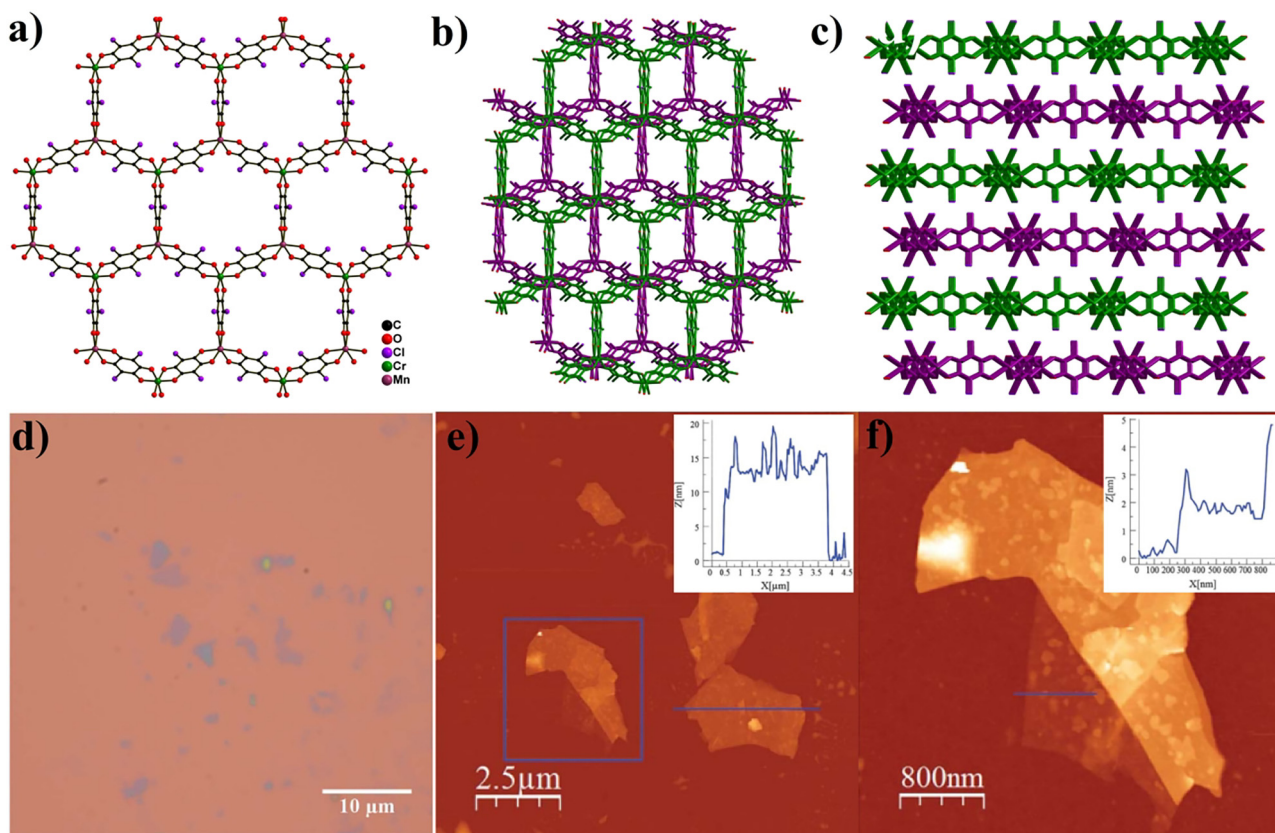
(continued on next page)

Table 1 (continued)

| Preparation method | Formular                                     | Crystal structure   | Space group               | Interlayer distance (Å) | Ref  |
|--------------------|--|---|---------------------------|-------------------------|--|
|                    | HfBTB  |    | $P2_1/m$ (11) -monoclinic | 17.27                   | [117]  |
|                    | M(TCPP)                                      |    | $Pmma$ (51)-orthorhombic  | ~9.3800                 | [82]<br>[84]<br>[85]<br>[38]<br>[120]<br>[124]<br>[126]<br>[127]<br>[41] |
|                    | NiCo-UMOFNs                                  |    | $P1$ (1)-triclinic        | 3D MOF                  | [41]   |
|                    | $[Ni_3(OH)_2(C_8H_4O_4)_2(H_2O)_4]$          |    | $P\bar{1}$ (2)-triclinic  | 7.4555                  | [43]<br>[44]   |
|                    | $[Co_2(OH)_2C_8H_4O_4]$                      |    | $C2/m$ (12)-monoclinic    | 3D MOF                  | [45]   |
|                    | $[Zn_3BDC_4]$                                |   | $C2/c$ (15)-monoclinic    | 3D MOF                  | [123]  |
|                    | $Hf_6(\mu_3-O)_4(\mu_3-OH)_4(H_2O)_4(BTE)_4$ |  | $Fmm2$ (42)-orthorhombic  | 3D MOF                  | [128]  |
|                    | M(TCPP)                                      |  | $Pmma$ (51)-orthorhombic  | 9.3800                  | [103]<br>[105]<br>[106]<br>[109]   |

the 3D superstructure with  $\pi$ -stacking between aromatic rings of the organic ligands, which results from the 2D layer stacking, has exhibited weak interlaminar interactions (Fig. 3b), making this compound an attractive candidate for the sonication-assisted exfoliation of ultrathin layers. The nanosheets thickness obtained from AFM image is about  $5 \pm 0.15$  Å, which conforms to that of the single-layer structure (Fig. 3c). In conclusion, this nanosheet is the first one-atom-thick MOFs nanosheet fabricated by sonication-assisted liquid exfoliation. Subsequently, many efforts have been made to explore the factors affecting sonication-assisted liquid exfoliation. In 2015, the same research group and their co-worker Gómez-Herrero had designed a new MOF  $[Cu(\mu\text{-pym}_2\text{S}_2)(\mu\text{-Cl})]_n$ , which also displayed weak interlaminar interaction in structure (Fig. 3d–e) [14]. Specifically, lateral size and thickness of the MOF nanosheets can be controlled through regulating exfoliation and centrifugation parameters using the same method. Moreover, comparisons of the AFM and optical images of MOF nanosheets indicate that the thickness of MOF nanosheets is about 2 nm (Fig. 3f). In summary, this is an efficient means to produce MOF nanosheets with dimensions of several hundred micrometers lateral and excellent controllable thickness.

Apart from the sonication time and centrifugation rate, another key factor influencing the exfoliation efficiency is the surface energy matching between the solvent and the bulk materials. Notably, Coleman and coworkers had verified the relationship of various solvents with the production quality of graphene from the same original graphite material [64]. Both experimental and theoretical results indicate that the matching relationship between materials and solvents has resulted in efficient exfoliation of the ultrathin nanosheets. In 2011, Xu et al. had successfully exfoliated the crystalline  $\{Zn(TPA)(H_2O)\cdot DMF\}_n$  into nanosheets (Fig. 4a–b) using the sonication-assisted liquid exfoliation in acetone [12]. The lateral dimension of nanosheets varies from 100 nm to 1  $\mu$ m (Fig. 4c). Noticeably, the 1.5 nm-thick nanosheets correspond to two MOF layers. Moreover, this MOF can be delaminated into nanosheets only under acetone, which can be attributable to the natural structural properties of this MOF. However, delamination has failed when other solvents or humid samples are used. In 2012, Rosseinsky reported a MOF  $[Zn(\text{Gly-Thr})_2]\cdot CH_3OH$ , which could also be exfoliated by sonicating the dried solid in acetone [15]. Moreover, in 2013, Kondo and Maeda had obtained the exfoliated MOF nanosheets (even the single-layer nanosheets) in a



**Fig. 2.** (a), (b) and (c) The structure of  $[\text{Mn}^{\text{II}}\text{Cr}^{\text{III}}(\text{Cl}_2\text{An})_3]^-$  in different view directions; Optical (d), and AFM (e and f) images of the exfoliated MOF nanosheets. Photo by M. Clemente-León and E. Coronado/CC BY 3.0.

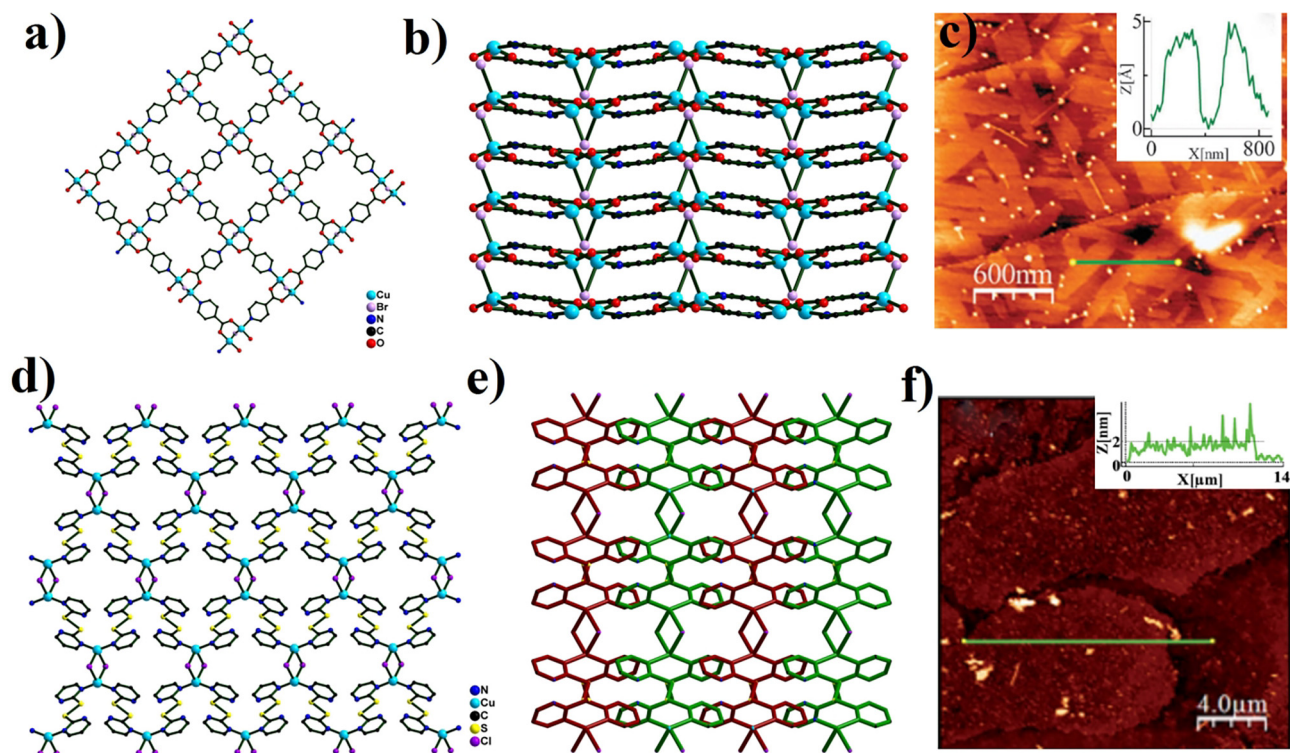


**Fig. 3.** (a) and (b) The structure of  $[\text{Cu}_2\text{Br}(\text{IN})_2]_n$  in different view directions; (c) Morphology of  $[\text{Cu}_2\text{Br}(\text{IN})_2]_n$  nanosheets; Copyright © 2010, Royal Society of Chemistry. (d) and (e) Structure of  $[\text{Cu}(\mu\text{-pym}_2\text{S}_2)(\mu\text{-Cl})]_n$  with different side view; (f) AFM image of  $[\text{Cu}(\mu\text{-pym}_2\text{S}_2)(\mu\text{-Cl})]_n$ . Photo by J. Gómez-Herrero and F. Zamora/CC BY 3.0.

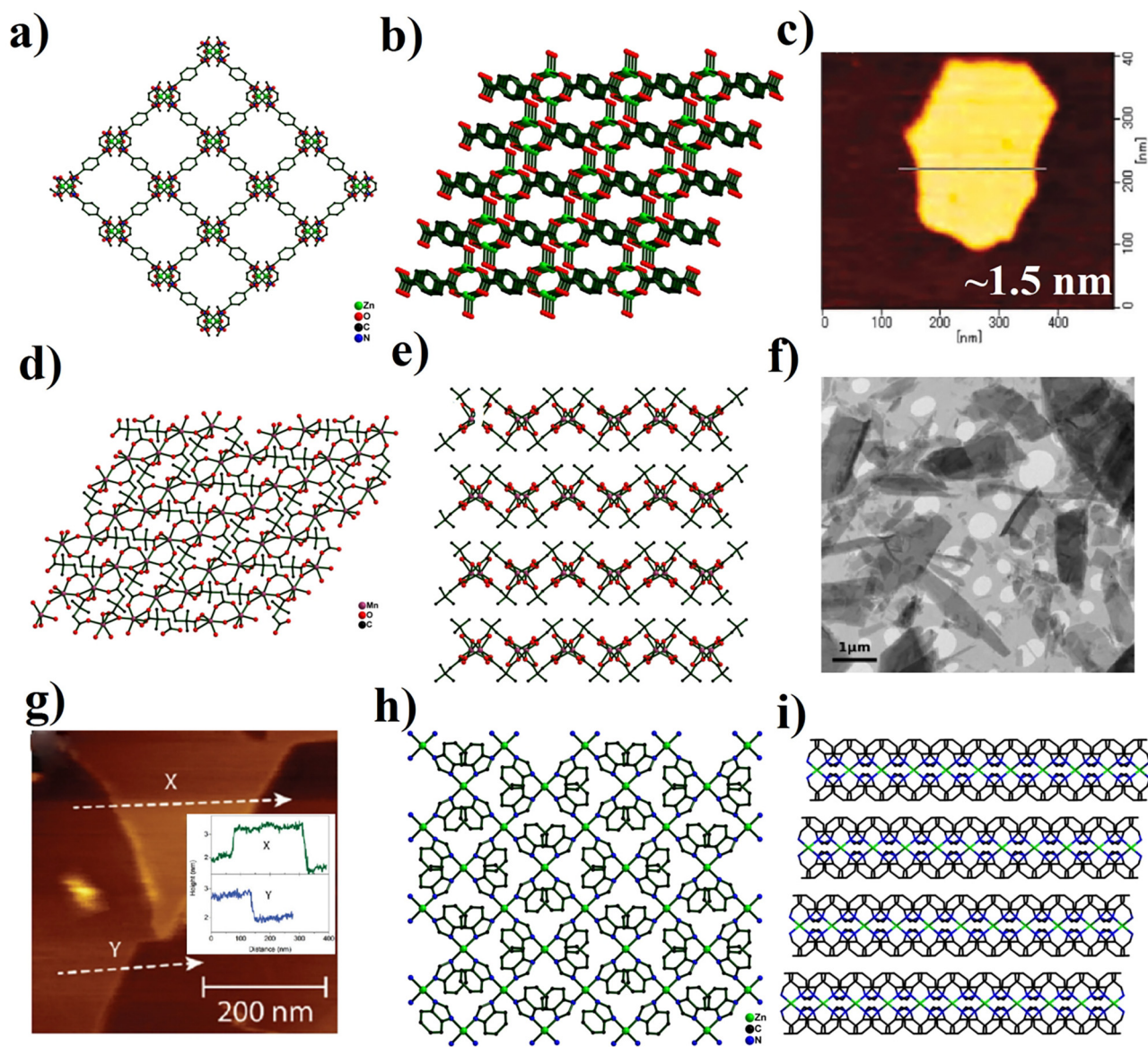


**Fig. 4.** (a) and (b) The framework of MOF-2; (c) The AFM image of a MOF-2 nanosheet. Copyright © 2011, Royal Society of Chemistry. (d) and (e) Crystal structure of Mn(C<sub>6</sub>H<sub>8</sub>O<sub>4</sub>)(H<sub>2</sub>O); (f) TEM image of the exfoliated nanosheets; (g) Two fully exfoliated unilamellar nanosheets of Mn(C<sub>6</sub>H<sub>8</sub>O<sub>4</sub>)(H<sub>2</sub>O); Copyright © 2012, American Chemical Society; (h) 2D layer and (i) 3D stacking structure of Zn<sub>2</sub>(bim)<sub>4</sub>.

mixture of organic solvents (acetone and ethanol) [16]. Hence, it can be suggested from the above analysis that, solvent plays a vital role in the exfoliation of bulk layered crystals, not only graphite but also MOFs.

Additionally, other solvents have also been explored for the exfoliation of MOFs into nanosheets [17–27]. Chemtham group had made a remarkable contribution to the exploration of MOF nanosheet preparation since 2012 [17–21]. To be specific, the solvents explored by their group included water [17], ethanol [19], acetonitrile, methanol, propanol, hexane, DMF [21], and THF. Moreover, the new 2D framework material MnDMS (Fig. 4d–e), which is weakly bound in the hybrid layers, can be exfoliated into nanosheets [17], with the thickness of unilamellar MOF nanosheets of about 1 nm (Fig. 4f–g). To explore the effects of solvents, other solvents (including THF, hexane, propanol, methanol, ethanol, and water) had been used as the exfoliation agents. The results suggest ethanol was the most efficient solvent to exfoliate the layers, which could also prevent the isolated films from subsequent

reassembly. Besides, the same authors had exfoliated several layered structures in their follow-up research [19]. Among them, ethanol was also used as the exfoliation agent, which could partly exfoliate ZnDMS into nanosheets, with thickness of approximately 100 nm and lateral size of about 10 μm. Differently, LiDMS was ultrasonicated in acetonitrile and could be exfoliated into much thinner nanosheets (<10 nm), but the lateral sizes of the exfoliated nanosheets retained at micron dimension. Nonetheless, the lateral sizes of the exfoliated nanosheets LiDMS, MnDMS and ZnDMS showed a decreasing trend, suggesting that not only solvents but also structure factors could impact the different lateral dimensions of ultrathin nanosheets. Besides, they also reported the preparation of ultrathin nanosheets from a series of layered bulk MOF crystals in ethanol solvent by ultrasonication through the coordination of 2,3-DMS and Mn/Co/Zn [20]. Typically, these compounds could be exfoliated and isolated into monolayer nanosheets.

In addition to the low boiling point solvents, in 2016, Chemtham and co-worker Foster had carried out sonication of



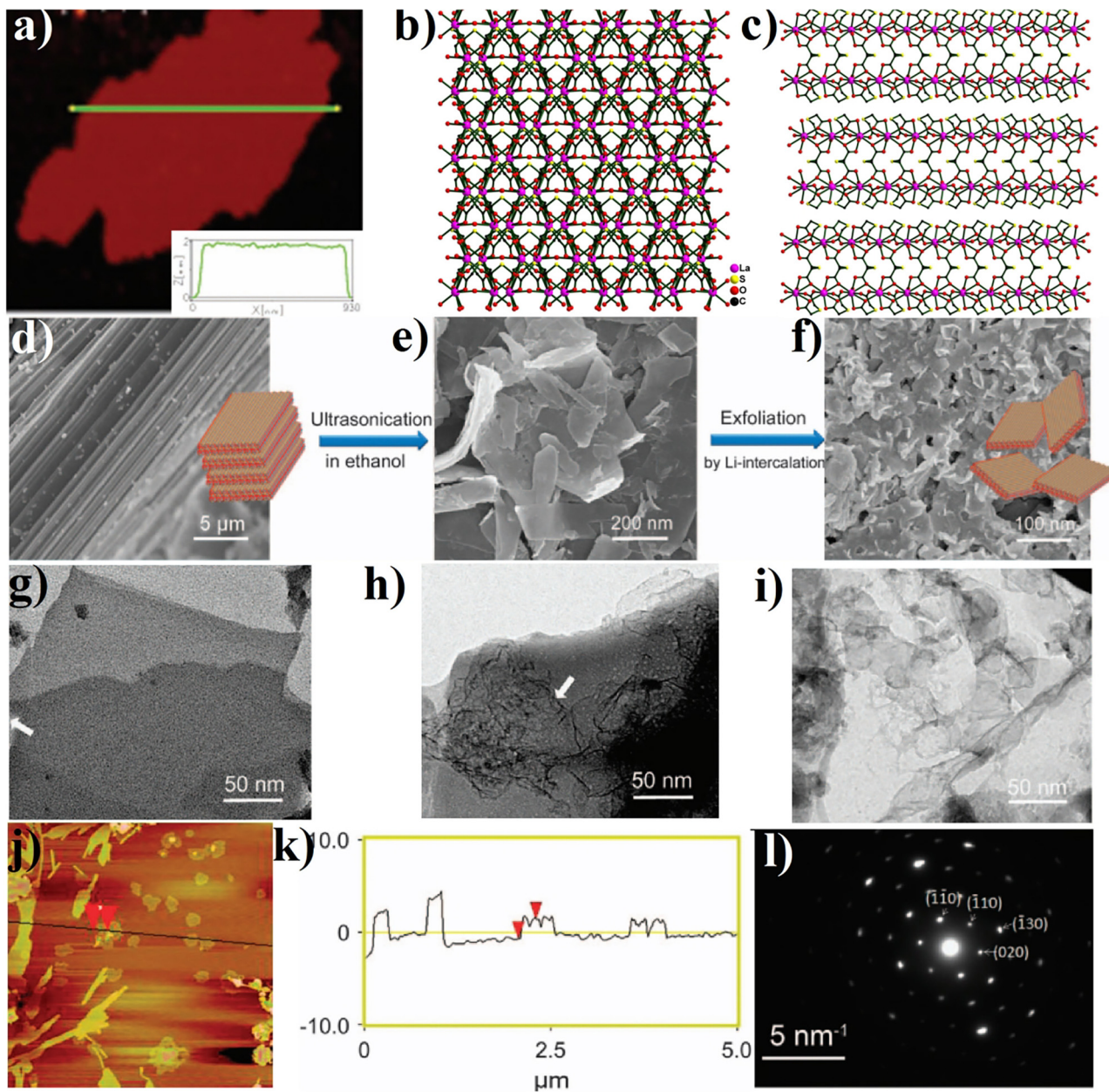


**Fig. 5.** (a) AFM of  $[\text{Cu}(\mu\text{-pym}_2\text{S}_2)(\mu\text{-Cl})]_n$ ; Copyright © 2013 WILEY-VCH Verlag GmbH & Co. KGaA, Weinheim. (b) and (c) Structural of the MOF-La; (d–i) Morphology of MOF-La nanosheets; (j and k) AFM results of MOF-La nanosheets; (l) SAED of MOF-La nanosheet. Copyright © 2017, Springer Nature.

MOFs in high boiling point solvents (such as DMF, water and DMF-water mixture) to obtain MOF nanosheet suspensions. This could be ascribed to the structural characteristics of the layered MOFs with metal-PW and alkyl-ether groups [21]. Specifically, the sizes of these nanosheets detected by AFM was at the nanometer scale (thickness: 2–30 nm; lateral size: 50–500 nm). That study was the first report on exfoliation assisted under different functionalities of the MOF nanosheets series. In addition, early in 2013, Maeda and co-workers had exfoliated the layered compounds  $\text{Ln}[(\text{HO}_3\text{P})_2\text{CH}-\text{C}_6\text{H}_4-\text{CH}(\text{PO}_3\text{H})(\text{PO}_3\text{H}_2)]\cdot 4\text{H}_2\text{O}$  ( $\text{Ln} = \text{La}, \text{Nd}$ ) and  $\text{Ln}_2[(\text{HO}_3\text{P})(\text{O}_3\text{P})\text{CH}-\text{C}_6\text{H}_4-\text{CH}(\text{PO}_3)(\text{PO}_3\text{H})]\cdot 8\text{H}_2\text{O}$  ( $\text{Ln} = \text{La}, \text{Nd}, \text{Gd}, \text{Dy}$ ), with DMF as the exfoliation agent. They had first obtained the lanthanide organophosphonate nanosheets [22].

Deviating from the typical liquid exfoliation method, Yang et al. had reported the efficient exfoliation of a 2D  $\text{Zn}_2(\text{bim})_4$  using a

two-step procedure [23]. Firstly, the wet ball-milling was applied on the crystals at 60 rpm, and secondly, the powder was sonicated in a mixture of methanol and propanol. It was found that methanol could easily penetrate into the layered  $\text{Zn}_2(\text{bim})_4$  under the assistance of wet ball-milling. Besides, propanol could hinder the overlapping of exfoliated nanosheets when it was adsorbed. Fig. 4h showed the 2D single-layer network structure and the 3D supermolecular architecture of  $\text{Zn}_2(\text{bim})_4$ . Moreover, AFM results confirmed that the greatest lateral dimensions of nanosheets could reach 1.5 mm and the thickness was 1.12 nm.

To date, the above-mentioned exfoliation method has been used in the preparation of a vast range of MOF nanosheets, which can be ascribed to the cheap and convenient process. Moreover, this method can successfully exfoliate almost all the layered bulk MOF materials into ultrathin nanosheets in the solvent.

### 2.1.3. Solvent-induced delamination exfoliation

Mechanical exfoliation using an adhesive tape and sonication-assisted liquid exfoliation can obtain the high-quality nanosheets and massive nanosheet suspensions, respectively. However, the exfoliation result seems to be uncontrollable when a mechanical force is applied to a bulk sample to obtain ultrathin nanosheets. Furthermore, it has been rarely reported that the layered bulk materials are exfoliated using chemical or solvent alone, which is called the solvent-induced delamination exfoliation method.

This unique method used to exfoliate bulk MOF crystals was first reported by Zamora and Delgado in 2013 [69]. After exposing to air under ambient humidity, the  $[\text{Cu}(\mu\text{-pym}_2\text{S}_2)(\mu\text{-Cl})]_n \cdot n\text{MeOH}$  crystals had undergone solvent exchange, which could yield 2D  $[\text{Cu}(\mu\text{-pym}_2\text{S}_2)(\mu\text{-Cl})]_n \cdot n\text{H}_2\text{O}$ . In this structure, the pyrimidine rings of  $\text{pym}_2\text{S}_2$  ligands, which had adopted the planar anti-conformation (Fig. 3d–e), had pointed outward the 2D plane layer. Besides, the 3D arrangement of this 2D plane layer would lead to voids in the adjacent layers; thus, the well-sized solvent molecules could easily occupy the voids and establish the weak hydrogen bonding interactions. It was clearly shown from the crystal structure that, the thickness of a crystal structure layer was approximately 8.5 Å. Notably, the crystals could be fully exfoliated only by immersion in a liquid solution, and such a rare phenomenon was proposed to be directly related to the structural characteristics. Moreover, the AFM images of  $[\text{Cu}(\mu\text{-pym}_2\text{S}_2)(\mu\text{-Cl})]_n$  indicated that the nanosheet thickness on the substrates ranged from 1.5 to 2.5 nm, reaching the single-layer level (Fig. 5a). To our knowledge, it was the first report regarding a layered MOF fully exfoliated solely by solvent-assisted interaction.

### 2.1.4. Exotic substance intercalation-assisted liquid exfoliation

Intercalating chemical ions/organic ligands into the interspace of MOF crystals is the basic idea to form the exotic substance-intercalated compounds. The ultrathin MOF nanosheets can be obtained in high yields, since the interactions between the 2D layers are weakened by intercalating exotic compounds. For instance, the famous 2D materials  $\text{MoS}_2$  and other TMDs have been successfully exfoliated using the ion interaction-assisted liquid exfoliation method. Early in the 1980s, Morrison and co-workers had already attempted to exfoliate TMDs into nanosheets using *n*-butyllithium [70]. The 2D layered materials can be successfully exfoliated by this method, as shown below: (i) The interspace between adjacent layers can be expanded, and the van der Waals interaction can also be weakened, thanks to the small ionic radius ions in the compound layers. (ii) The produced  $\text{H}_2$  contributes to exfoliating the bulk materials. Therefore, the ultrathin nanosheets can be obtained after sonication in the solvent, so long as the ion-intercalated compounds are successfully prepared.

Nevertheless, such method is rarely reported to exfoliate the layered bulk MOF crystals [28,29,71]. In 2017, Xia first reported the successful preparation of lanthanide-based MOF nanosheets [28]. Fig. 5b had displayed the 2D layer structure of MOF-La (Fig. 5c). There are two steps in exfoliating MOF-Lns. Firstly, sonicating the layered MOF-Lns in ethanol to obtain the nanoparticles; and the multi-layer nanosheets can then be obtained with the increase in ultrasonication time (Fig. 5d–e). Secondly, the MOF-Ln nanosheets can be fully exfoliated according to the Li-ion intercalation method (Fig. 5f–i). As previously mentioned, this method is associated with an advantageous feature, which is that a large amount of monolayer or few-layer nanosheets can be produced. Meanwhile, results from SAED and AFM indicated that the thickness of the exfoliated crystalline MOF-Ln nanosheets was 2 nm (Fig. 5j–l), and a majority of the exfoliated MOF-Ln nanosheets showed a small size of 500 nm × 500 nm.

Also in 2017, Zhou, Xu and Jiang co-workers had obtained the MOF nanosheets through a so-called ligand interaction-assisted

liquid exfoliation method [29]. To obtain the ultrathin MOF nanosheets, new intercalated MOFs should be formed first of all by incorporating 4,4'-dipyridyl disulfide into MOF crystals. Subsequently, the disulfide bonds in the structure had fractured under sonication, resulting in the exfoliation of the MOF crystals and production of plenty of ultrathin MOF nanosheets. To sum up, the ligand interaction-assisted liquid exfoliation method is verified to be a versatile approach to synthesize MOF nanosheets.

## 2.2. Bottom-up methods

### 2.2.1. Hydro-solvothermal syntheses

The hydro/solvothermal synthesis method is a classical and widely used strategy to synthesize MOF single crystals or other inorganic compounds as a result of its various merits [72–79]. Interestingly, this method has also been widely used to synthesize ultrathin MOF nanomaterials [80–86]. Kitagawa had first synthesized several hundred lateral sized Cu-TCPP nanosheets about 15 nm in thickness (Fig. 6a–c) [82]. Additionally, Lotsch et al. had synthesized ultrathin MOF nanosheets after subsequent exfoliation using the surfactant-mediated method [83]. Firstly, stacks of nanosheets were self-assembled under the assistance of surfactant cetyltrimethyl-ammonium bromide, resulting in a hybrid highly crystalline lamellar substructure with a lattice period of about 8 nm (Fig. 6d). Secondly, the hybrid material was then sonicated in organic solvents, eventually yielding the nanosheets (10 nm in thickness) with lateral sizes of 10–100 nm (Fig. 6e). In recent years, Lin and co-workers reported several Zr/Hf-MOF 2D metal-organic layers by a modulator-assisted synthetic method [39,81,129,132]. By using this method, the ultrathin 2D MOF nanosheets not only can be large scale-up synthesis but also multi-functionalized by organic ligands and metal ion/metal cluster secondary building units design.

Zhang's group had prepared several kinds of MOF nanosheets (<10 nm in thickness) [84,85], among which, the Zn-TCPP nanosheets were synthesized for the first time, and their 2D layered sheets consisted of one TCPP ligand as well as four  $\text{Zn}_2(\text{COO})_4$  in PW metal modes [84]. To limit the dimensional growth of MOFs, polyvinylpyrrolidone was attached onto the 2D plane surface as the surfactant to control the formation of ultrathin MOF nanosheets (Fig. 6g). The resultant Zn-TCPP nanosheets showed micrometre ( $1.2 \pm 0.4 \mu\text{m}$ ) large lateral size and relatively thin thickness of about  $7.6 \pm 2.6 \text{ nm}$  (Fig. 6h–i), which indicated  $8 \pm 3$  layers of the Zn-TCPP. Similarly, Co-TCPP, Cd-TCPP and Cu-TCPP could also be obtained through this general method. Additionally, the ultrathin bimetallic MOF M-TCPP(Fe) (M = Cu, Co, or Zn) nanosheets were also successfully prepared by this method for the first time [85].

Beyond heating the regular autoclaves or synthetic vials in an oven, it's worth mentioning that ultrasonic is also energy input in a hydro-solvothermal synthesis. Because long time continuous ultrasound not only can generate localized hot point but also increase molecular vibration, which creates a special hydro-solvothermal synthetic environment to synthesize 2D MOF nanosheets. For example, Tang's group prepared ultrathin NiCo bimetal-organic framework nanosheets by sonicating the colloidal solution of reactants for 8 h (40 kHz) under airtight conditions [41]. Owing to their ultrathin nature, NiCo-UMOFNs can be well dispersed in the aqueous solution for several months. The 2D morphology of the NiCo-UMOFN has been verified by four reflections indexed into (h0l), which assigned to the (200), (001), (201) and (201) crystallographic planes, in the small angle X-ray scattering pattern. The thickness of the 2D MOF nanosheet is about 3.1 nm, corresponding to four or three layers. Hence, the 2D shape nanosheet with uniform thicknesses and the exposed metal atoms also meet the requirement for MOFs-based catalysts.

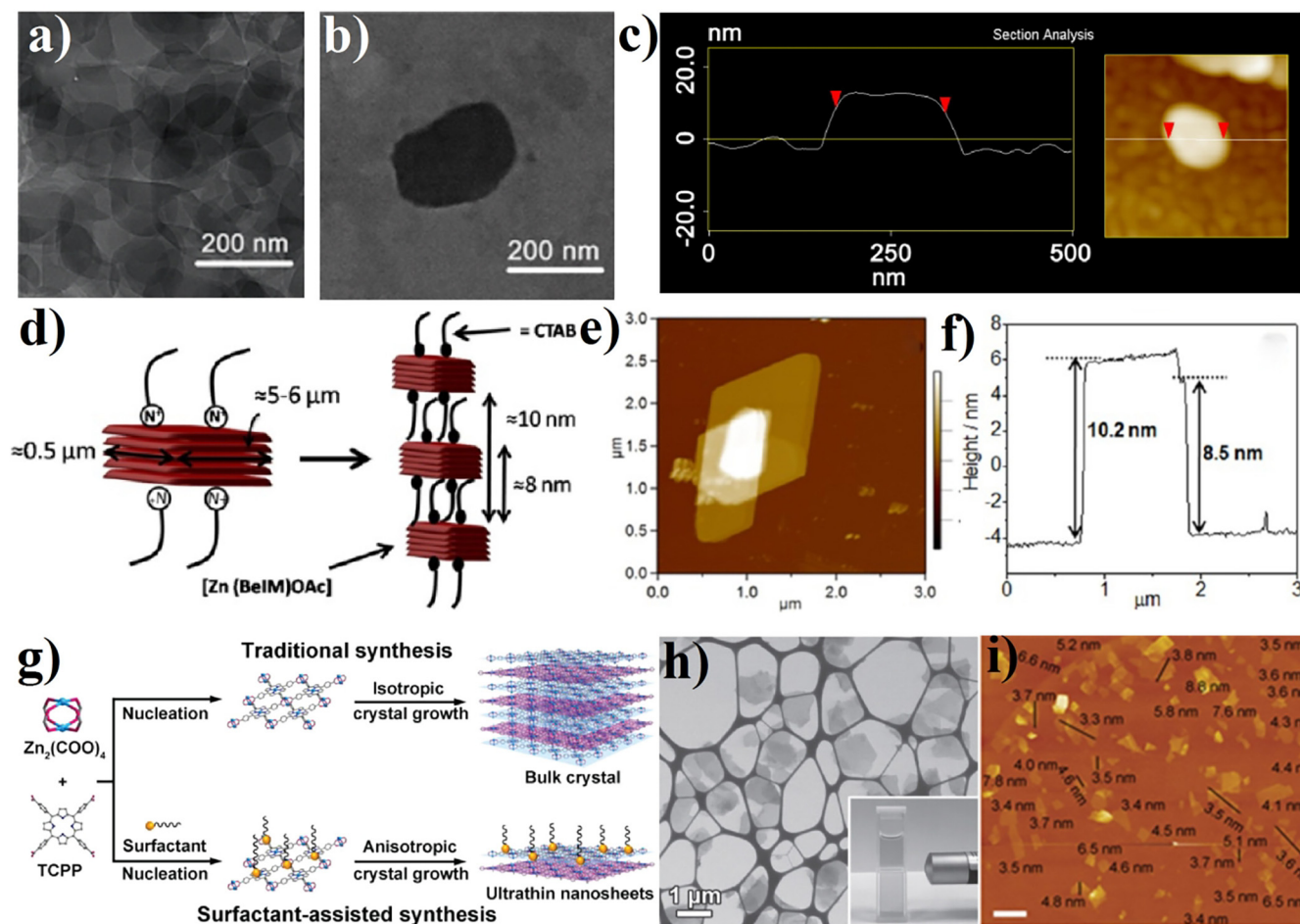


**Fig. 6.** (a–c) Morphology of the Cu-TCPP nanosheets; Copyright © 2012, American Chemical Society. (d) Composite mesostructure of [Zn(BeIM)OAc]; (e) and (f) AFM results of [Zn(BeIM)OAc]; (g) The synthetic strategy of MOF; Copyright © 2013, American Chemical Society. (h) STEM image of Zn-TCPP nanosheets. (i) AFM images of Cu-TCPP nanosheets. Copyright © 2015 WILEY-VCH Verlag GmbH & Co. KGaA, Weinheim.

### 2.2.2. Interface-mediated syntheses

The interface-mediated synthesis method is a technique that grows the ultrathin nanosheets, especially the MOF nanosheets, through the gas/solid, liquid/air or liquid/liquid interface. As a promising route to prepare MOF nanosheets, a superior interface is a key factor, which is typically used as a “surface” for reaction, so as to assemble the extended sheets, while metal ions can also be supplied from the solid metal substrate or the solution. Lin, Barth, Kern and Iannuzzi et al. attempted to elaborate the synthesis process at atomic scale [87–95]. Early in 2003, Lin, Barth, and Kern firstly used the gas/solid surface to synthesize MOF nanosheets layers under ultra-high vacuum deposition conditions [96]. For the gas/solid interface synthesis method, there are some key factors: 1) some flat metal surface, such as Cu (100), Ag (100) or Ag (111), and Au (111), should be prepared firstly; 2) a UHV chamber with base pressures of less than  $5 \times 10^{-10}$  mbar is required. Then, the metal atoms and organic ligands were deposited under the above mentioned key synthesis conditions. Finally, the substrates with deposited MOF structural components should be annealed several minutes to promote the reaction between the two components to construct 2D MOF nanosheets. Not only the synthesized 2D MOF nanosheets showed some unique coordination modes by using this synthesis method, but also the close contact between the metal solid substrate and 2D MOF nanosheets may offer great advantages in some special application fields.

To date, the air/water and liquid/liquid interfaces are two common useful interfaces to synthesize MOF nanosheets [30–36]. In 2013,  $\pi$ -conjugated nickel bis-(dithiolen) nanosheets were synthesized through the interface-mediated method (Fig. 7a) [30]. In general, the conventional liquid-liquid interface-mediated synthesis method can only produce films with the thickness of several micrometers (Fig. 7b); nonetheless, the single-layer (0.6 nm) or few-layer nanosheets can be obtained through reducing the amount of reagents in the gas-liquid interface (Fig. 7c–e). Soon after, the  $\pi$ -conjugated coordination nanosheets comprised of bis (aminothiolato)nickel were also synthesized in the gas-liquid and liquid-liquid interfaces, respectively. Particularly, the synthesis of single-layer nanosheets (about 0.6 nm in thickness) was also controllable [31]. In 2015, the same research group had described another MOF nanosheet consisting of dipyrin ligand (Fig. 7f) [35]. Similarly, the typical liquid/liquid interface-mediated synthesis method could only obtain multi-layer compounds 700 nm in thickness (Fig. 7g–j). Meanwhile, the few-layer nanosheets and single-layer nanosheets 10 mm in lateral size were obtained through the air/liquid interfacial reaction (Fig. 7k).

In 2015, Gascon and co-workers had exploited a three-layer synthesis strategy to synthesize the copper 1,4-benzenedicarboxylate MOF (Fig. 7l–m) [36]. Three solutions were employed to control the medium diffusion to influence the growth kinetics of MOFs, and the nanosheets 5–25 nm in thickness and micrometer in lateral size could be produced in a high yield

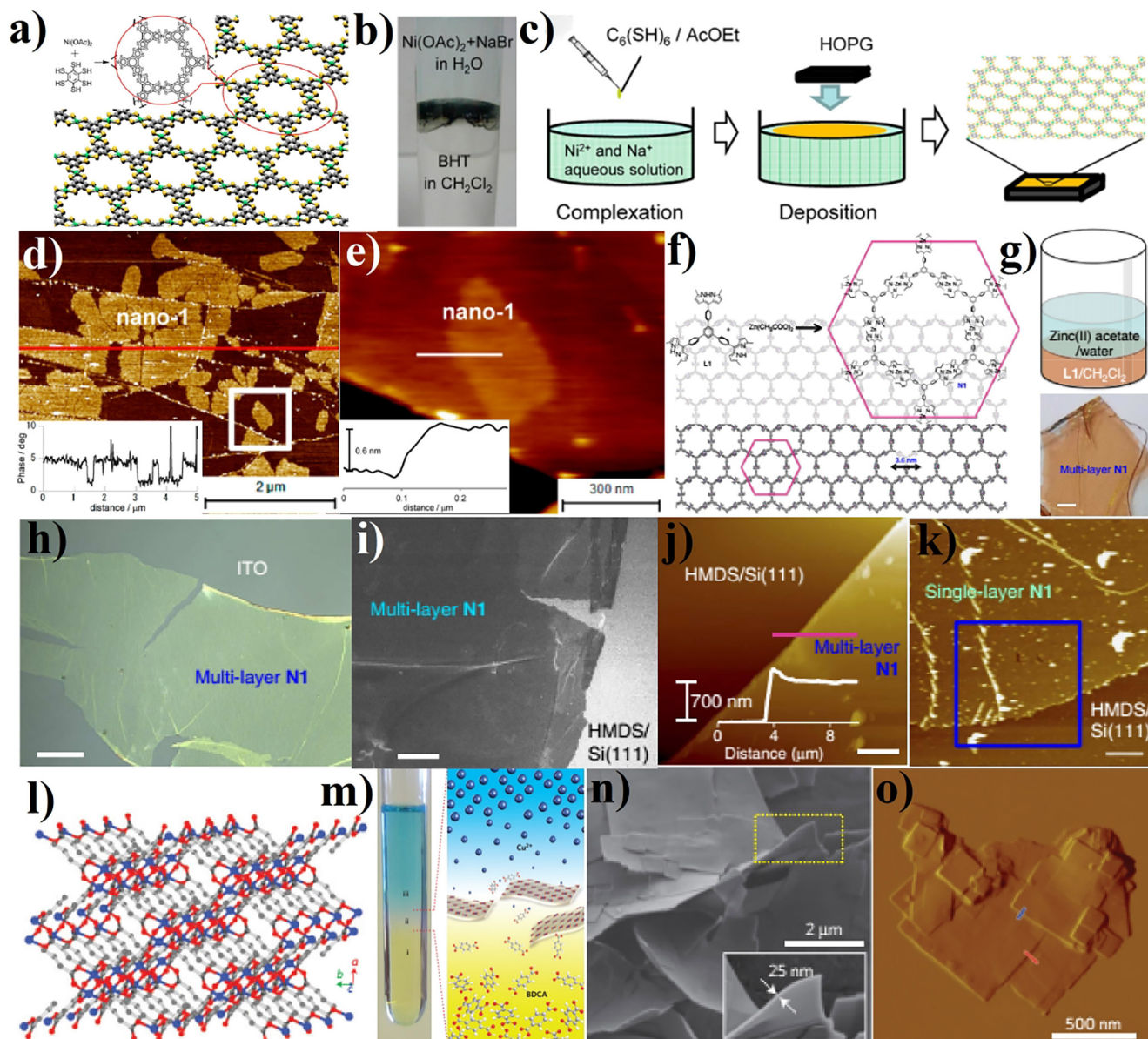


**Fig. 7.** (a) Crystal structure of the nickel bis(dithiolene); (b) Photograph of the synthesis result; (c) The synthesis process of the nanosheets; (d) and (e) AFM results of the synthetic nanosheets; Copyright © 2013, American Chemical Society. (f) Structure of the bottom-up nanosheet; (g) The synthesized multi layer nanosheet; (h) Optical image of the nanosheet; (i) FE-SEM image on HMDS/Si(1 1 1); (j, k) AFM results of the nanosheets; Copyright © 2015, Springer Nature. (l) The structure of the CuBDC; (m) Synthetic schematic diagram of CuBDC nanosheets; (n) SEM and (o) AFM results of CuBDC nanosheets. Copyright © 2014, Springer Nature.

(Fig. 7n–o). Notably, the thickness of CuBDC nanosheets could be well controlled by changing the solvent species and reaction temperature. Certainly, the solution containing  $\text{Cu}^{2+}$  and BDCA precursors could slowly diffuse into the middle region under the static reaction conditions at room temperature, resulting in the production of more thinner MOF nanosheets. Furthermore, other layered MOF nanosheets could also be successfully obtained using this synthetic technique by changing the metal centers and ligands.

Taken together, such interface-mediated synthesis method is linked with two distinct superiorities. Firstly, the ultrathin nanosheets with large scale and high yield can be obtained; secondly, the synthesized MOF structures are diversified through adopting different metal ions and organic ligands. Therefore, such interface-mediated synthesis method may be an effective means to broaden the resulting nanosheets diversity.

### 2.2.3. Langmuir-Blodgett (LB) method

The LB method is a proven technology, by which the well-organized monolayers are fabricated on air/liquid surfaces and can be easily transferred onto solid substrates. Unlike the interface-mediated method that adjusts diffusion reactions by controlling molecular dynamics, the LB method relies on instruments to guarantee that the surface pressure-promoting reactions only take place on the air/liquid interface. Such a technique has been employed to successfully assemble various molecular systems into the well-ordered 2D arrays [97–100]. Moreover, composing with the L-B-L growth technique, this method is in favor of synthesizing supermolecular architectures, which has been applied to fabricate MOFs [101–103]. Such method bases on the ordered arrangement of reaction components as a result of chemical reaction, which is characterized by its merit that the oriented films can be acquired.

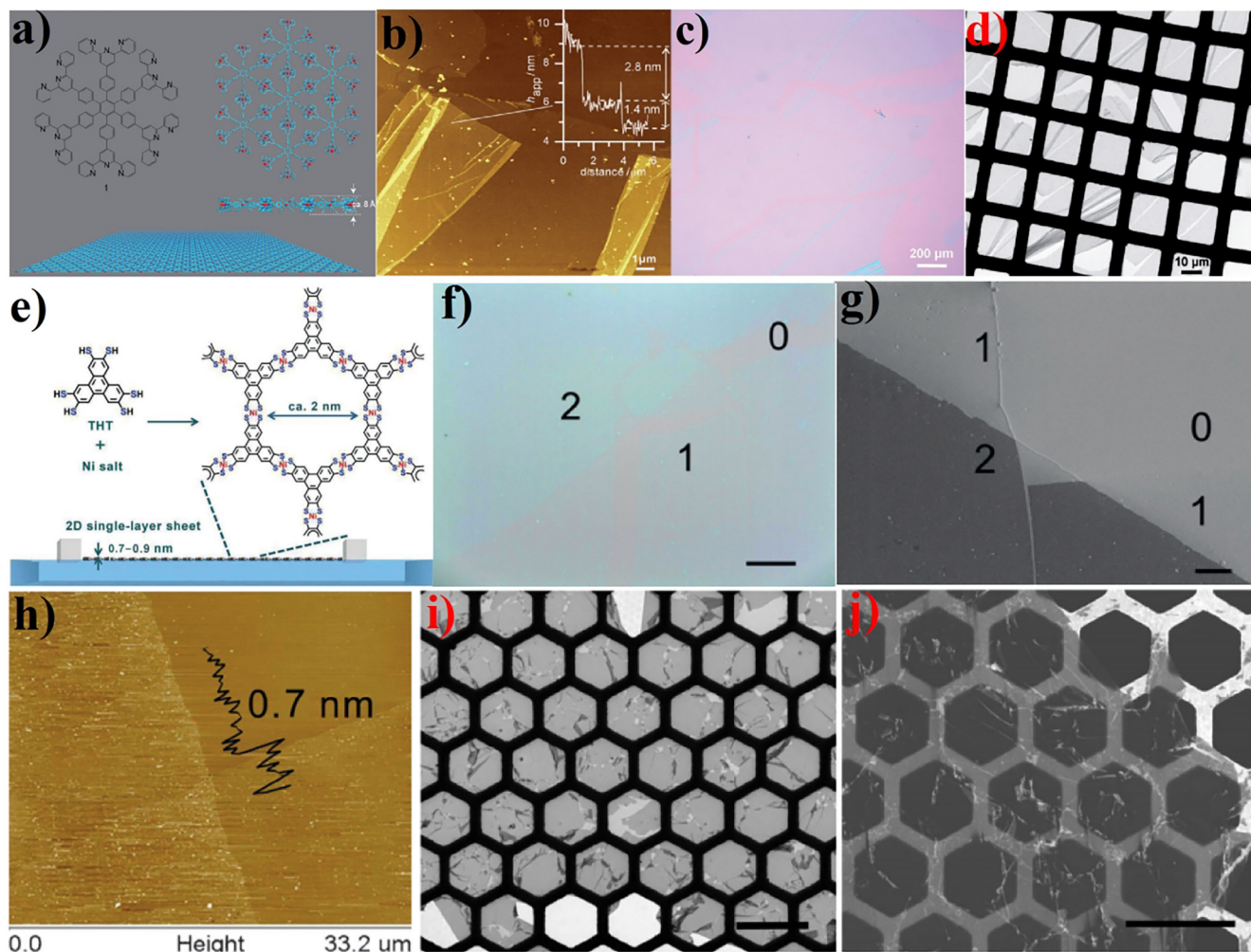


**Fig. 8.** (a) Chemical structure of the two-dimensional network; (b) AFM result of the nanosheet; (c) Optical micrograph image of the nanosheets; Copyright © 2011 WILEY-VCH Verlag GmbH & Co. KGaA, Weinheim. (e) Synthesis of single-layer 2D MOF nanosheet using the LB method on air/water interface; (f) Optical microscopy images of the 2D MOF sheets; (g) SEM images of the single- and multi-layer nanosheets; (h) AFM results of the nanosheets; (i) and (j) Morphology of nanosheets on Cu grids. Copyright © 2015 WILEY-VCH Verlag GmbH & Co. KGaA, Weinheim.

Kitagawa and Makiura had demonstrated the adept integration of both the LBL growth and the LB method in a modular fashion to fabricate crystalline MOF on the solid surface [104]. Meanwhile, other examples have also proven that the LB method is an effective approach to fabricate ultrathin MOF films or large-scale nanosheets [40,105–111].

In 2011, Schlöter had published a pioneer work on synthesizing the monolayer large-scale MOF nanosheets on the water/air interface [105]. Typically, such free-standing monolayer sheets contained the hexa-functional tpy-based  $D_{6h}$ -symmetric monomers (Fig. 8a) and  $\text{Fe}^{2+}$ . In the detailed process, chloroform of ligands was dropwise deposited on the top of an aqueous  $\text{Fe}^{2+}$  solution. Then, the low-solubility ligands would polymerize on the water surface after chloroform evaporation. Subsequently, the ligands were compressed and aggregated on the interface under a  $10 \text{ mN m}^{-1}$  surface pressure. Finally, the monolayer large-scale MOF nanosheets  $[\text{Fe}_2(\text{tpy})^{4+}]_n$ , ( $0 < n < 3$ ) were obtained, which could be transferred on the solid substrates. Concretely, the as-prepared nanosheets were about 1.3 nm in thickness and macroscopic size in the lateral dimension, which could even stably span holes with pore size of  $20 \times 20 \text{ nm}^2$  or greater (Fig. 8b–d). Besides, similar nanosheets with  $\text{Ru}^{2+}$  or  $\text{Zn}^{2+}$  ions could also be obtained. Typically, the first monolayer MOF nanosheet ( $>500 \times 500 \text{ nm}^2$ ) was successfully synthesized in this work. Three years later, a series

of MOF monolayers had been prepared by the same group through the reactions of oligo-functional terpyridine-based ligands with  $\text{Pb}^{2+}$ ,  $\text{Zn}^{2+}$ ,  $\text{Co}^{2+/3+}$ , and  $\text{Fe}^{2+}$  ions [109].

Soon, nickel bis(dithiolene) complexes single-layer nanosheets were synthesized by Feng et al. using the LB method [40]. Similarly, the submonolayer of THT ligand was formed on the surface for the first time. After reaction with the diffuse aqueous nickel salts solution, the large-area MOF nanosheets were fabricated, with the thickness of about 0.7 nm (Fig. 8e and h). It was obvious that the synthesized sheet was stable enough to span over the Cu grids as a free-standing structure (Fig. 8i–j).

Hence, the LB method is an effective approach to synthesize the ordered and large-area thin nanosheets, which also possesses some other merits. Specifically, (i) the large-scale nanosheets can be synthesized on the liquid surface; (ii) the straightforward preparation and single-layer isolation can be transferred onto any substrates; and (iii) the large-scale single-layer nanosheets can reduce the difficulty in device preparation.

In summary, only part of MOF nanosheets can be prepared by using all above-mentioned method. For the top-down method, in order to get large-scale few-layer nanosheets, the parent bulk materials with sufficient bulk size are recommended. Because the top-down method will more or less destroy the bulk materials in order to overcome the interaction between layers. On the other

hand, the MOF structure with larger distances in the adjacent layers, or intercalated molecules can be prepared as MOF nanosheets in preference to use the top-down method with external force and chemically assisted external force. While, in the case of the MOF with a bigger conjugate system through the whole plane structure, the interaction force between these  $\pi$ -system layers is too strong to be broken easily. Hence, the bottom-up method is a good choice to synthesize the MOF nanosheets for them.

It's worth mentioning that these preparation methods almost have no structural change or disruption to the bulk MOF, so the nanosheets may not only maintain the chemical and physical properties of bulk MOFs, but also broaden their application fields based on their high surface-to-volume ratio, high exposed catalytic sites, the superiority of surface engineering strategies, and high exposure surface.

### 3. Applications of MOF nanosheets

The preparation methods described above have successfully prepared a wide variety of MOF nanosheets with different structures, sizes, thicknesses. The combining of the features of MOF with 2D nano-structures sometimes upgrades the performances of MOF nanosheet materials and gives them a variety of intriguing applications, including (i) separation, where MOF nanosheets play key roles in the highly selective and efficient separation; (ii) catalysts, in which tuned structure of MOFs, accessible active-sites, and fast-charge transport in MOF nanosheets are propitious to catalyze the organic reaction, OER and HER; (iii) sensing, in which fluorescence (optical sensors), biocompatibility (biosensors), and electrochemical property (electromechanical sensors) of MOF nanosheets can construct the signal transduction network or create a physical interface for signal transduction; and (iv) energy conversion and storage, in which high-density active sites, rapid ion/electron transport and ultrathin nanostructures in MOF nanosheets will facilitate electrolyte ion diffusion while improving the high performance of supercapacitors. Moreover, the remarkable performances for enzyme inhibitor of MOF nanosheets have also been demonstrated recently. In this section, the recent advancements of MOF nanosheets will be overviewed in terms of separation, catalysis, sensing, and energy storage.

#### 3.1. Separation

Noteworthy, the sizes and dimensions of cavities/pores in MOF nanosheets can be tuned, thanks to the numerous available choices of organic and inorganic components for MOFs construction, which can further regulate the interaction between guest molecules and MOF nanosheets. In addition, the high specific surface area and good dispersibility of MOF nanosheets render them the active materials for independent separation or in composition with other materials.

##### 3.1.1. Gas separation

MOF nanosheets are the most suitable components for high performance molecular sieve membranes, owing to their ultrathin characteristics and large aspect ratio. In 2014, Yang [23] had reported using the 1-nanometer-thick MOF nanosheets [ $\text{Zn}_2(\text{bim})_4$ ] as a functional layer on  $\alpha\text{-Al}_2\text{O}_3$  disk surface for  $\text{H}_2/\text{CO}_2$  separation. Typically, the highly crystalline  $\text{Zn}_2(\text{bim})_4$  nanosheets with BET of  $112.4 \text{ m}^2/\text{g}$  (5.6 times higher than that of bulk materials) were disorderly assembled onto the  $\alpha\text{-Al}_2\text{O}_3$  disk surface and formed a membrane by using the hot-drop coating technology. This process is only applicable to flexible  $\text{Zn}_2(\text{bim})_4$  nanosheets due to their large lateral area and thin enough thickness, which is not possible for layered bulk  $\text{Zn}_2(\text{bim})_4$ .

Membrane separation was then tested using the  $\text{H}_2/\text{CO}_2$  mixture, which exhibited excellent molecular sieve performance. Typically, the  $\text{H}_2/\text{CO}_2$  selectivity could be increased to 291 at the  $\text{H}_2$  permeance of 3760 gas permeation units (GPUs). Furthermore, the structure-performance relationship was also investigated, which suggested that the orderly stacked MOF nanosheets had impeded the penetration of  $\text{H}_2$ , resulting in a reduction in the membrane performance. Recently, the [ $\text{Zn}_2(\text{benzimidazole})_3(\text{OH})(\text{H}_2\text{O})$ ] $_n$  nanosheets [37] were also selected to fabricate the sub-10-nm-thick ultrathin membrane for  $\text{H}_2/\text{CO}_2$  separation. Typically, the improved performance was realized by the size sieving effect. Concretely, 166 separation factors were attained at  $200^\circ\text{C}$ , and the  $\text{H}_2$  permeance was as high as  $8 \times 10^{-7} \text{ mol m}^{-2} \text{ s}^{-1} \text{ Pa}^{-1}$  (Fig. 9).

Moreover, Gascon and coworkers had incorporated MOF nanosheets into polyimide (PI) matrices, and the resultant MOF-polymer composite membranes were used for  $\text{CO}_2/\text{CH}_4$  separation [36]. The freestanding CuBDC nanosheets in the membrane with high aspect ratio had presented isotropic crystal morphology and were uniformly distributed at all depths with preferential orientation perpendicular to the gas flux direction (Fig. 10). Additionally, the exposed surface area of nanosheets-CuBDC@PI was approximately 10 times higher than that of bulk-CuBDC@PI at the equal concentration of filler. On this account, the nanosheets-CuBDC@PI had displayed better  $\text{CO}_2$  separation selectivity than those of polymeric membrane and bulk-CuBDC@PI. Notably, under the same condition, the separation performance could reach up to 180% of that of polymeric membrane and even eight times of that of bulk-CuBDC@PI. Remarkably, the separation selectivity would be obviously increased with the addition in pressures, which might result from the counteracting plasticization effect of MOF nanosheets. Their study had underlined the importance of orientation and distribution of MOF nanosheets in polymer films. In 2017, similar studies were conducted by Zhao [112] and Bae [113], which showed improved  $\text{CO}_2/\text{CH}_4$  separation performance. Besides, these MOF nanosheet composite membranes also presented unique separation behaviors, thanks to the favorable orientation and higher distribution of MOF nanosheets.

Additionally, Zhao and coworkers had demonstrated a mixed matrix membrane (MMM) composed of [ $\text{Cu}_2(\text{ndc})_2(\text{dabco})$ ] $_n$  nanosheets for  $\text{H}_2/\text{CO}_2$  separation performance in 2015 [114]. Specifically, these microporous jungle-gym-like MOFs (Fig. 11a–c) were obtained through the bottom-up method, and then subsequently blended with polybenzimidazole to yield MMMs. These lamellar MOF nanosheets fillers were stacked orderly, thus giving rise to better  $\text{H}_2/\text{CO}_2$  separation performance than that of the nanocube and bulk fillers. To be specific, the selectivity of NS@PBI-20 could achieve 26.7 under the  $\text{H}_2$  permeability of 6.13 Barrers at  $35^\circ\text{C}$  under 5 bars.

In 2017, the same group [115] had prepared different nanometer-thick (4, 12, and 40 nm) molecular sieving membranes comprised of MAMS-1 [ $\text{Ni}_8(5\text{-bbdc})_6(\mu\text{-OH})_4$ ] nanosheets onto the  $\text{Al}_2\text{O}_3$  substrates (Fig. 11d–i). These membranes had exhibited favorable  $\text{H}_2/\text{CO}_2$  separation performances, which could be attributed to the orderly arranged MAMS-1 nanosheets. The 4 nm membrane showed small separation factor at the given viscous flow, and the 12 nm membrane presented the increased separation factors of  $34 \pm 5$  and the best  $\text{H}_2$  permeance of  $6516 \pm 990$  GPUs. By contrast, the 40 nm membrane had possessed the increased separation factors of  $235 \pm 14$ , but with compromised  $\text{H}_2$  permeance of  $553 \pm 228$  GPUs (Fig. 11j), since the excess MOF nanosheets had increased gas travel distance but hampered  $\text{H}_2$  flowing. On the other hand, the MAMS-1 membranes also displayed long-term stability. Moreover, the insignificant performance loss of 40 nm membrane was also evaluated for the 10,000 min separation (Fig. 11k). Remarkably, these well-ordered MAMS-1

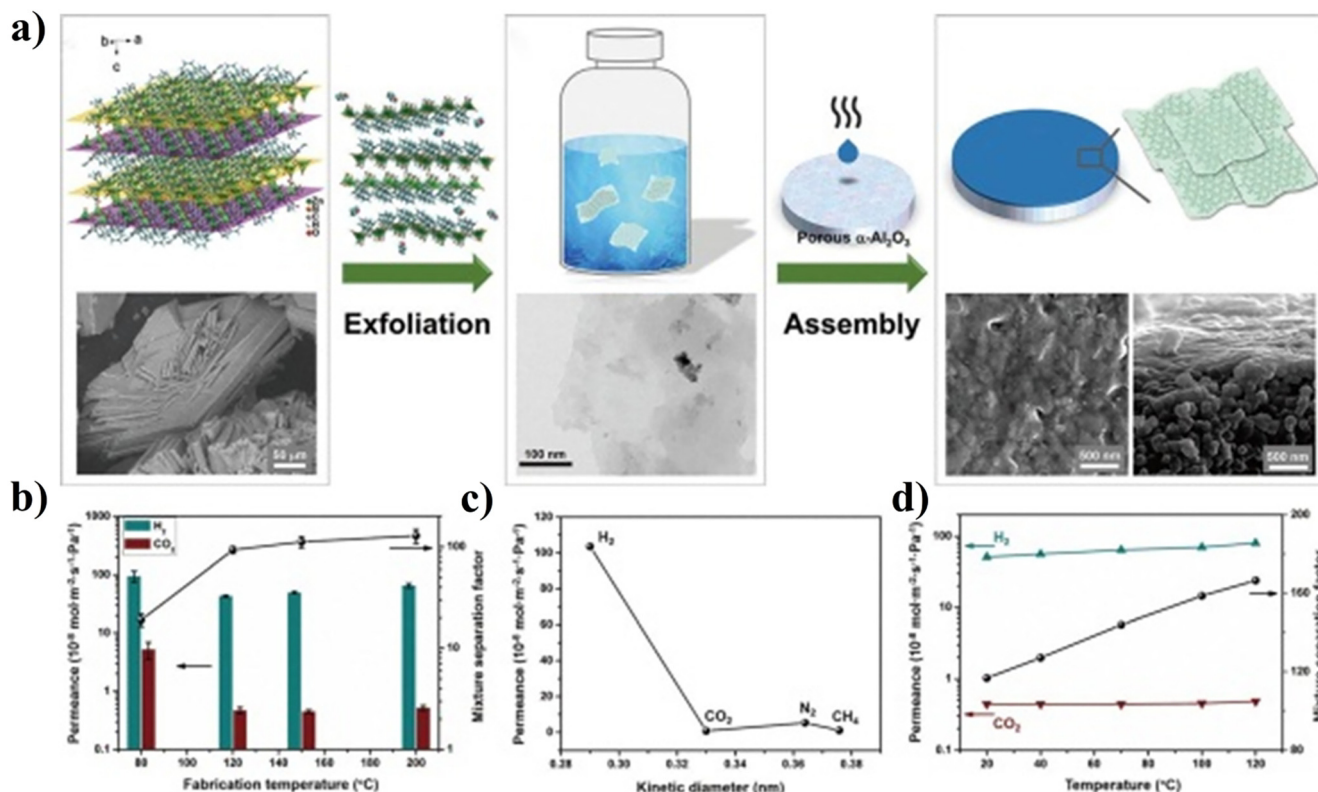


**Fig. 9.** MOF nanosheets membrane for H<sub>2</sub>/CO<sub>2</sub> separation properties. (a) The fabrication of Zn<sub>2</sub>(Bim)<sub>3</sub> nanosheet membrane; (b) Binary gas separation performance; (c) Single gas permeation; (d) Influence of different temperatures on H<sub>2</sub>/CO<sub>2</sub> permeability of Zn<sub>2</sub>(Bim)<sub>3</sub> nanosheet membrane and mixture SF Copyright © 2017 Wiley-VCH Verlag GmbH & Co. KGaA, Weinheim.

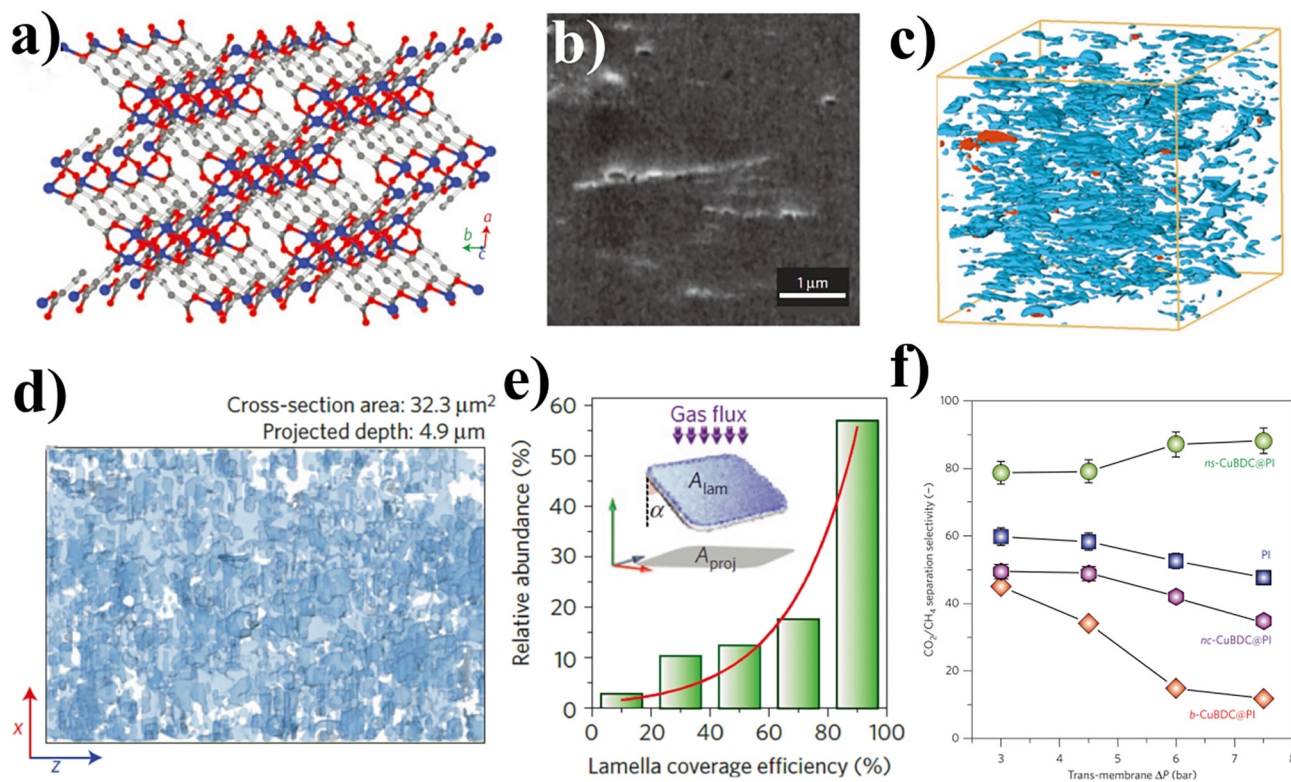


**Fig. 10.** Gas separation of MOF-polymer composite membranes. (a) The structure of CuBDC; Morphology (b: cross-sections SEM, c: segmented FIB-SEM tomograms and d: Full projections) of CuBDC-polymer composite membranes; (e) Lamella cover efficiency of MOF nanosheets; (f) Separation selectivity of CO<sub>2</sub>/CH<sub>4</sub> at 298 K. Copyright © 2014, Springer Nature.

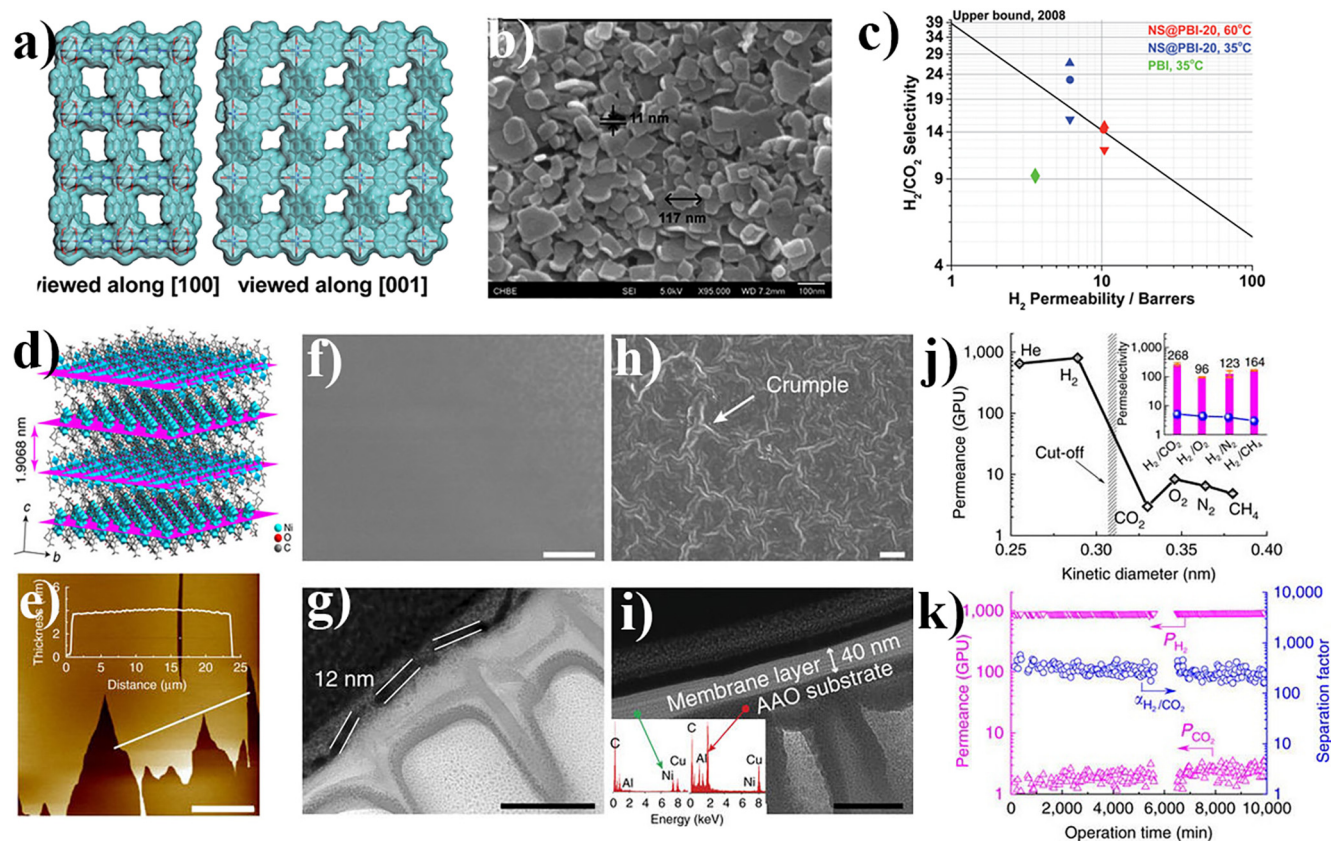


**Fig. 11.** Mixed matrix membranes of MOF nanosheets for  $\text{H}_2/\text{CO}_2$  separation. (a) The structure and (b) FE-SEM images of  $[\text{Cu}_2(\text{ndc})_2(\text{dabco})]_n$  nanosheets; (c)  $\text{H}_2/\text{CO}_2$  selectivity of NS@PBI-20. Copyright © 2015, Royal Society of Chemistry. (d) Structure and (e) morphology of MAMS-1 nanosheets; (f, g) FE-SEM images of 12-nm and (h, i) 40-nm MAMS-1 membranes; (j) Gas permeation of the 40-nm membrane; (k) Continuous  $\text{H}_2/\text{CO}_2$  separation test of 40-nm membrane at room temperature. Copyright © 2017, Springer Nature.

membranes had presented reversed thermo-switchable  $\text{H}_2$  permeation, indicating that  $\text{H}_2/\text{CO}_2$  separation was affected by temperature. Typically, the highest separation factors (2.45) could be achieved at 20 °C, which were different from those (~5) at 100 °C.

### 3.1.2. Nanofiltration

Nanofiltration of membrane is a highly energy efficient and cost-effective thermal separation technique. Notably, a nanofiltration membrane was fabricated with the selected Zn-TCP(Fe) nanosheets as the nanometer-thick active layers whereas polycations as the cross-linker [38], owing to its superior structural stability and strong stacking ability (Fig. 12a). More importantly, this membrane had exhibited excellent organic dyes separation performance thanks to the well packed MOF nanosheets in the thin active layers (Fig. 12b–d). To be specific, the good permeability of small organic dye was detected to be  $4243 \text{ L m}^{-2} \text{ h}^{-1} \text{ bar}^{-1}$ , and over 90% small organic dyes were rejected (Fig. 12e–f). In addition, salt rejection of 20%–40% could also be demonstrated in the membrane at 0.01 bar pressure. This finding has broadened a pathway to the future applications of porous MOF nanosheets, especially in water purification or solvent filtration.

## 3.2. Catalysts

MOF nanosheets allow for not only rapid mass transport but also superior electron transfer, both of which benefit the electrocatalysis. Meanwhile, the inherent porous structure and ubiquitous metal active centers in MOF nanosheets can also improve the catalysis efficiency while promoting the reaction rate. In addition, MOF nanosheets can efficiently guarantee the catalytic activity and

recycling of catalysts thanks to the natural properties of homogeneous catalysts with well-defined active site density as well as the heterogeneous catalysts with good durability. All of these advantages render MOF nanosheets an excellent candidate for acquiring the high performance electrocatalytic/heterogeneous catalytic systems. Therefore, this section will emphasize the latest development of catalytic reactions based on MOF nanosheets, including the high-performance electrocatalysts for OER and HER, together with heterocatalysis for organic reactions.

### 3.2.1. Electrocatalysis

The development of OER and HER using efficient catalysts has posed significant challenges for energy conversion technology. Tang had reported using the ultrathin Ni-Co MOF sheets (NiCo-UMOFNs) to efficiently catalyze OER [41]. After deposition of the bimetallic NiCo-UMOFNs (approximately 3-nm in thickness) (Fig. 13a–d) onto the copper foam, this modified electrode had displayed extremely low onset potential (~1.42 V), which is much better than bulk NiCo-MOFs electrodes (~1.48 V). Remarkably, NiCo-UMOFNs showed stabilized, high-efficient and fast OER reaction kinetics, as reflected in the smaller Tafel slope ( $42 \text{ mV dec}^{-1}$ ), higher turnover frequency ( $0.86 \text{ s}^{-1}$ ), higher faradaic efficiency (99.3%) and sustained current density (Fig. 13e). Such results had suggested oxygen evolution performance with high selectivity (Fig. 13f). On the other hand, the coordinatively unsaturated metal centers might result in the high catalytic activity of NiCo-UMOFNs. Moreover, the interaction between Ni and Co metal atoms in the ordered MOF structures was another key cause. Typically, the interaction between water and  $\text{Ni}^{2+}$  site would be enhanced due to electron transfer from  $\text{Ni}^{2+}$  to  $\text{Co}^{2+}$ . Electron density from  $\text{Ni}^{2+}$



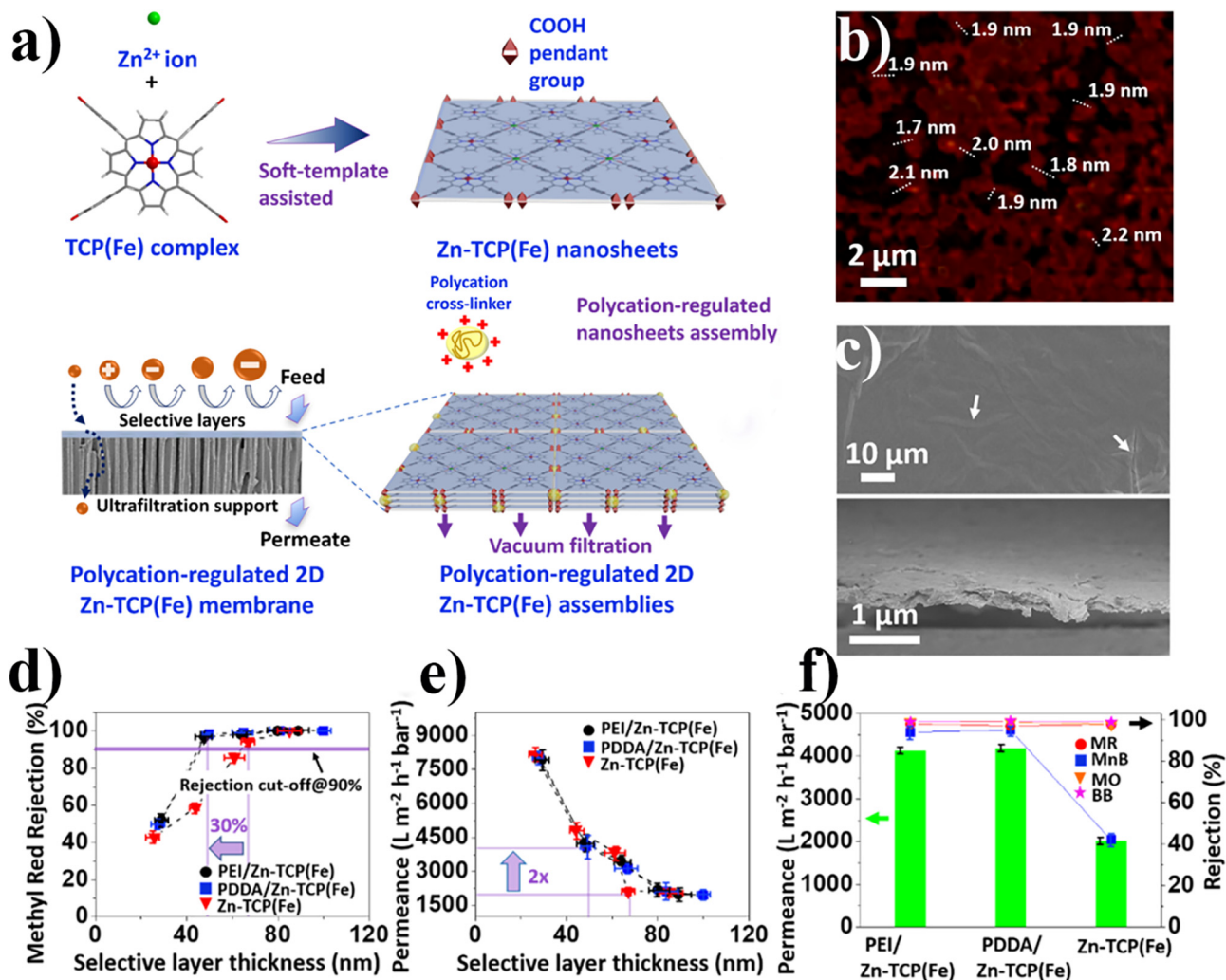


**Fig. 12.** MOF nanosheets membrane for nanofiltration. (a) Preparation of polycationic Zn-TCP(Fe) membrane; (b, c) Morphology of Zn-TCP(Fe) nanosheets and layers; (d–f) Separation and permeance performances of polycation regulated membranes fabricated by three kinds of MOF nanosheets. Copyright © 2017, American Chemical Society.

could be accepted by the  $e_g$ -orbitals of  $\text{Co}^{2+}$  compared with  $\text{Ni}^{2+}$  ( $\text{Co}^{2+} = d^7$  versus  $\text{Ni}^{2+} = d^8$ ). In turn, the lower energy barrier would be provided, since the oxidized nickel could more easily undergo electron transfer from water.

The 2D single-layer sheet of nickel bis(dithiolene) compounds (THTNi 2DSP sheet) was an excellent example of electrocatalytic HER of MOF nanosheets (Fig. 14a–b), as reported by Feng and co-workers [40]. Highly efficient electrocatalytic HER performance could be detected after deposition of large-area ( $>1 \text{ mm}^2$ ) free-standing nanosheets (0.7–0.9 nm thick) onto the rotating disk electrode (Fig. 13c). Apart from small onset overpotential (110 mV) and relatively low Tafel slope ( $80.5 \text{ mV decade}^{-1}$ ), this THTNi 2DSP sheet catalyst also displayed moderate operating overpotential under both acidic ( $413 \text{ mV}$  at  $10 \text{ mA cm}^{-2}$ ) and alkaline ( $574 \text{ mV}$  at  $10 \text{ mA cm}^{-2}$ ) conditions. All these efficient performances could be attributed to the uniformly distributed Ni-S units in THTNi 2DSP sheets for high catalytic efficiency and the large aspect ratio of single layer MOF nanosheets for the accessible active center.

Soon after, three forms of 2D single-layer (THAT-M, M = Co and Ni) MOF nanosheets (Fig. 14d) had been prepared as catalysts for HER by the same group [116]. These THAT-M MOF nanosheets consisted of  $\text{MS}_2\text{N}_2$ ,  $\text{MS}_4$  and  $\text{MN}_4$  complexes, which exhibited diminishing HER activity following the order of  $\text{MS}_2\text{N}_2 > \text{MN}_4 > \text{MS}_4$ .

Experimental results and DFT calculations indicated that the M@N site was the preferential place for protonation. Moreover, a synergistic effect from the coordination of metal, N and S would promote the addition/desorption of  $\text{H}_2$ , thus significantly accelerating the HER kinetics.

Zhao and coworkers had fabricated ultrathin MOF nanosheet array electrodes for efficient electrocatalytic water splitting [117]. Distinct from the above-mentioned methods directly depositing MOF nanosheets onto the electrode, they had fabricated  $\text{Ni}_{0.8}\text{Fe}_{0.2}(\text{C}_{12}\text{H}_6\text{O}_4)(\text{H}_2\text{O})_4$  (NiFe-MOF) nanosheet array on nickel foam surface through the in-situ growth method (Fig. 15a–c). This method was superior in that, firstly, the insulating binders were eliminated; secondly, the hierarchical porosity facilitated the mobility of  $\text{H}_2$ ,  $\text{O}_2$  or water during electrocatalysis; and thirdly, 2D nano-structuration of NiFe-MOF nanosheet array (thickness of  $\sim 3.5 \text{ nm}$ , lateral size of  $\sim 4100 \text{ nm}$ ) on the nickel foam could enhance the electrical conductivity of the whole electrode while maintaining the accessible active sites in nanosheets with large specific surface area. Therefore, compared with Bulk NiFe-MOF and Ni-MOF array, the as-prepared NiFe-MOF/NF material had exhibited superior performance in electrocatalytic OER (Fig. 15d–e), which also had good stability and low overpotential ( $240 \text{ mV}$  at of  $10 \text{ mA cm}^{-2}$ ). The turnover frequency could reach  $3.8 \text{ s}^{-1}$  even

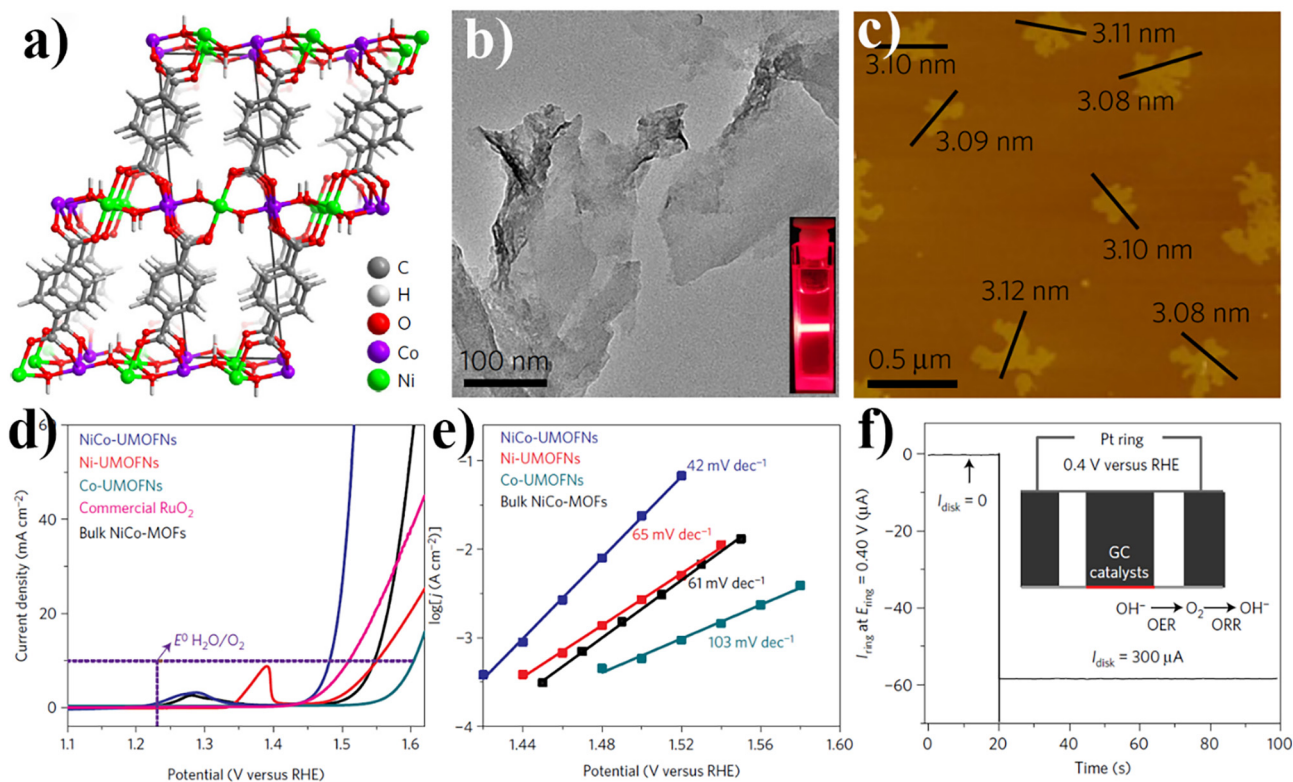


**Fig. 13.** MOF nanosheet for electrocatalytic OER. (a–c) Structure and morphology of NiCo-UMOFNs; Electrocatalytic OER properties (d: Polarization curves and e: Tafel plots) of NiCo-UMOFNs and comparison of related materials. (f) Faraday efficiency testing of NiCo-UMOFNs. Copyright © 2016, Springer Nature.

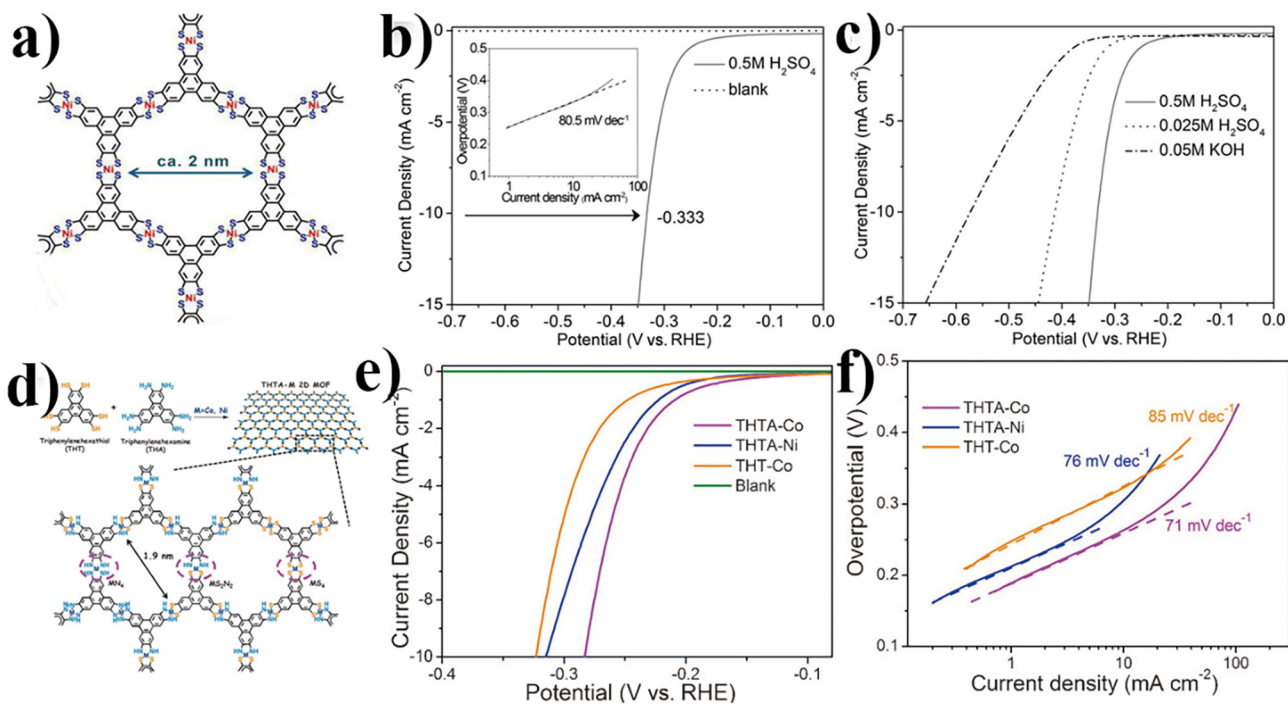


**Fig. 14.** MOF nanosheet for electrocatalytic HER. (a) Structure of the THTNi 2DSP complexes; (b, c) Polarization curves of THTNi 2DSP sheet under different solutions. Copyright © 2015 Wiley-VCH Verlag GmbH & Co. KGaA, Weinheim. (d) Schematic synthesis of single-layer 2D MOF nanosheets; electrocatalytic HER (e: polarization and f: Tafel plots) of 2D MOFs. Copyright © 2017 Wiley-VCH Verlag GmbH & Co. KGaA, Weinheim.

at an overvoltage of 400 mV. Remarkably, this NiFe-MOF/NF material was highly active for overall water splitting and HER (Fig. 15f). Taken together, such a strategy has taken full advan-

tage of MOF nanosheets and thus improved the electrocatalytic performance, which serves as a good example of how to fully develop and utilize MOF nanosheets.

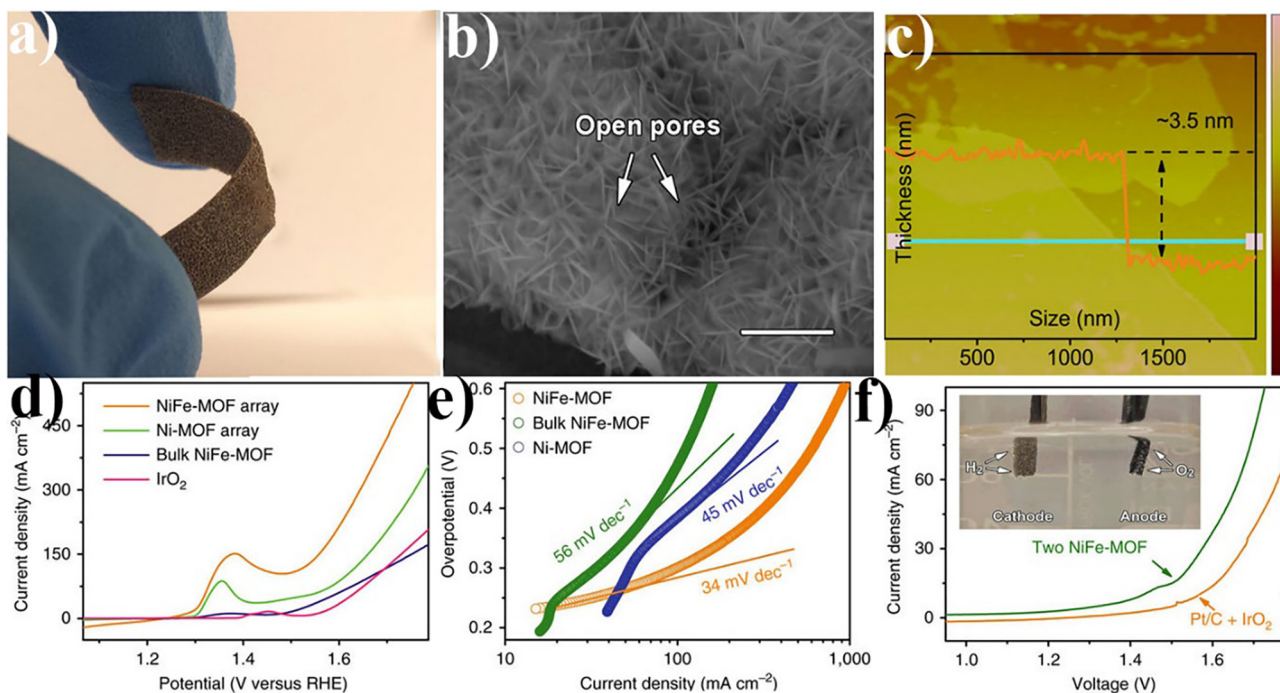


**Fig. 15.** MOF nanosheet for electrocatalytic water splitting. Morphology (a: Optical image, b: SEM images and c: AFM image) of NiFe-MOF electrodes; Electrocatalytic OER (d: LSV plots and e: Tafel plots) of NiFe-MOF electrodes; (f) LSV plots of full electrolytic cell and optical image of water splitting. Copyright © 2017, Springer Nature.

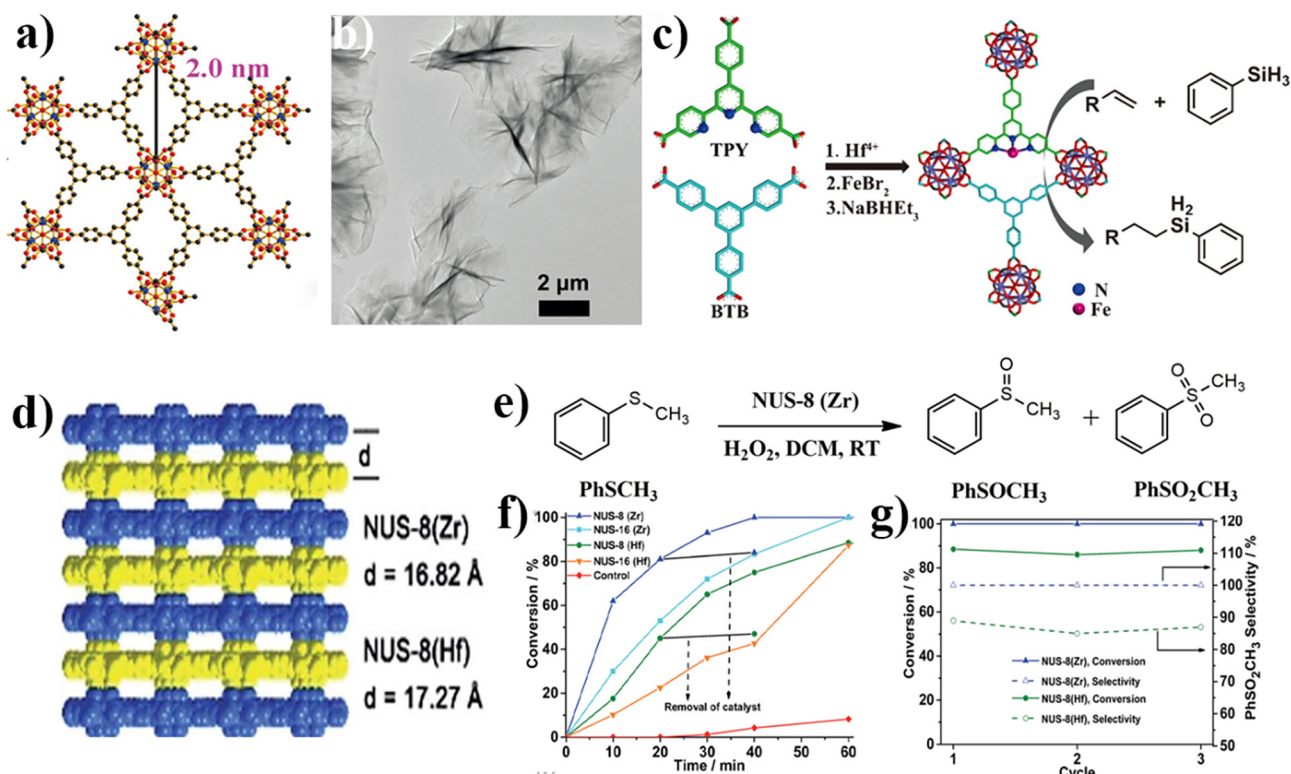


**Fig. 16.** MOF nanosheets for catalyzing organic reaction. (a) Structure of  $[\text{Hf}_6\text{O}_4(\text{OH})_4(\text{HCO}_2)_6(\text{carboxylate})_6]$ ; (b) TEM image of  $\text{Hf}_6\text{O}_4(\text{OH})_4-(\text{HCO}_2)_6(\text{BTB})_3$  nanosheets; (c) Preparation of Fe-TPY-MOL catalyst. Copyright © 2016 WILEY-VCH Verlag GmbH & Co. KGaA, Weinheim. (d) Structure of NUS-8; (e) Thioanisole oxidation reaction catalyzed by NUS-8(Zr); (f) Kinetic study and (g) cycle performance of thioanisole oxidation. Photo by D. Zhao/CC BY 3.0.

### 3.2.2. Organic reaction

MOF nanosheets not only inherit the advantage of bulk MOF catalysts (such as homogeneous catalytic site and porosity for

size-selection), but also possess the characteristics of 2D nanomaterials, like large special surface area and accessible active sites. All these features are beneficial for catalyzing organic reaction

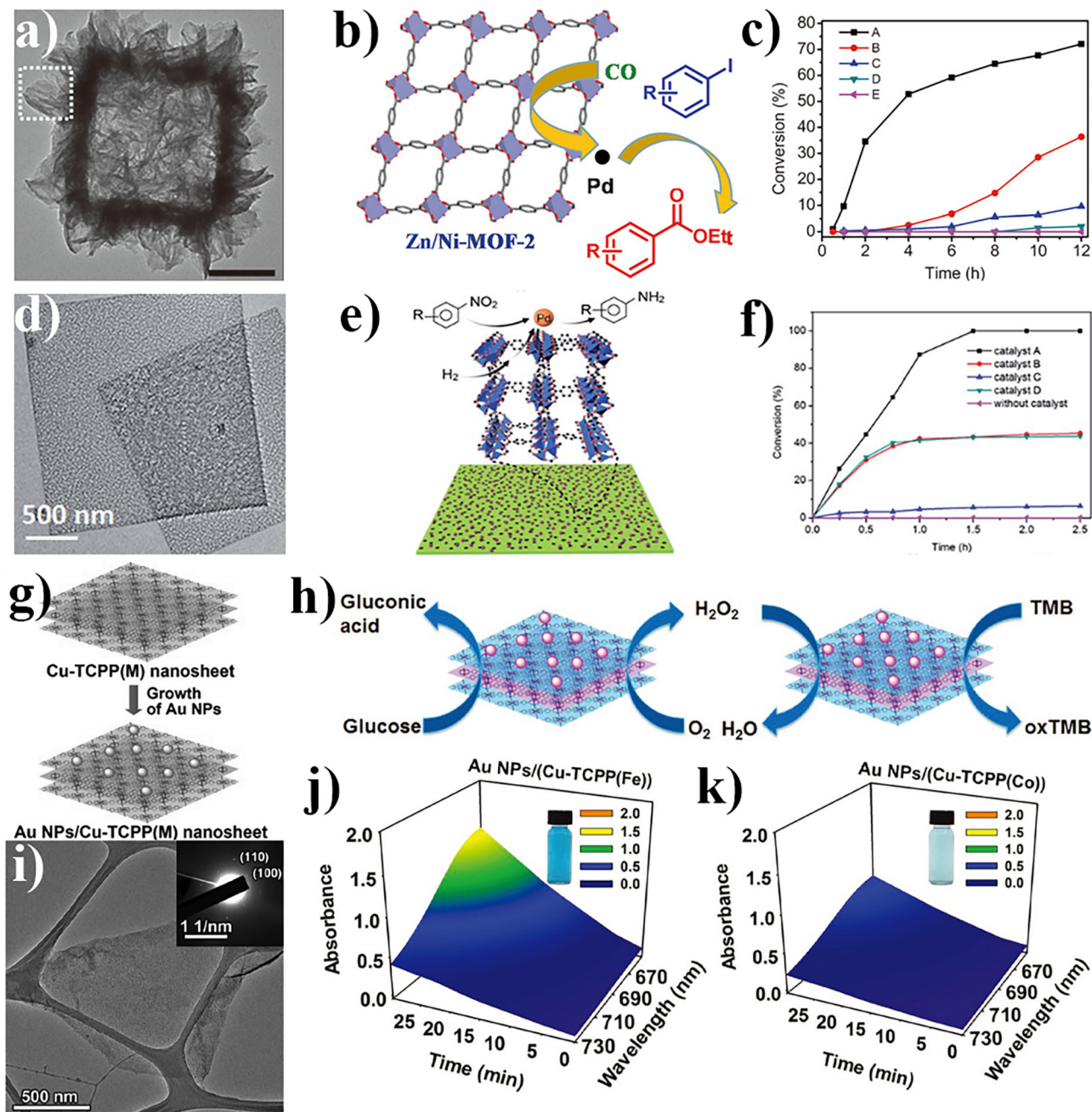


**Fig. 17.** MOF nanosheets for catalyzing organic reaction and biomimetic catalysis. (a) Morphology of Zn/Ni-MOF-2 NAHNS; (b) Alkoxycarbonylation of aryl halides reaction and (c) the conversion vs time. Copyright © 2014 WILEY-VCH Verlag GmbH & Co. KGaA, Weinheim. (d) HRTEM images of Pd-H-MOF-5 nanosheets; (e) Reduction reaction of nitroarene and (f) the conversion as a function of time. Photo by X. Wang/CC BY 3.0. (g) Sketch of synthesis and (i) TEM of Au NPs/Cu-TCPP (M) (M = Fe, Co) nanosheets; (h) The cascade reaction of enzyme-mimetic; (j) and (k) Absorption vs time spectra of the solution. Copyright © 2017 WILEY-VCH Verlag GmbH & Co. KGaA, Weinheim.

[39,118]. Lin and coworkers had developed a single-site Fe-TPY-MOL catalyst from a self-supporting MOF nanosheet [Hf<sub>6</sub>(μ<sub>3</sub>-O)<sub>4</sub>(μ<sub>3</sub>-OH)<sub>4</sub>(HCO<sub>2</sub>)<sub>6</sub>(BTB)<sub>2</sub>] (Fig. 16a–b) [39].

Compared with traditional MOFs with low catalytic activity, this Fe-TPY-MOL catalyst with accessible catalytic sites displayed a sterically protective environment, which could also afford the highly active and reusable heterocatalysis (Fig. 16c) [119]. Fe-TPY-MOF1 has not conversion and Fe-TPY-MOF2 shows low yield (30%), because their 3D structure limits the diffusion of the substrates and product. Differently, the Fe-TPY-MOL with 0.02% catalyst loading could efficiently catalyze the hydrosilylation of styrene, resulting in 100% conversion rate and acquisition of the pure anti-Markovnikov product over 48 h. Moreover, the turnover

number was as high as ~5000. Importantly, this MOF nanosheet catalyst could be recycled four times and exhibit good stability. Remarkably, almost all substrates could generate the pure anti-Markovnikov products, indicating that MOF nanosheets within uniformly distributed Fe-TPY species were advantageous for improving catalytic selectivity. In 2017, Zhao and coworkers [118] had synthesized a Zr/Hf MOF nanosheet (NUS-8) (Fig. 16d), which was subsequently employed to catalyze the oxidation reaction of thioethers. The NUS-8 nanosheet with alleviated framework strain presented excellent catalytic activity and selectivity and was superior to their bulk MOF counterparts with 3D interlocked structure, which could be ascribed to the advantage of MOF nanosheets as heterogeneous catalyst with accessible active sites that

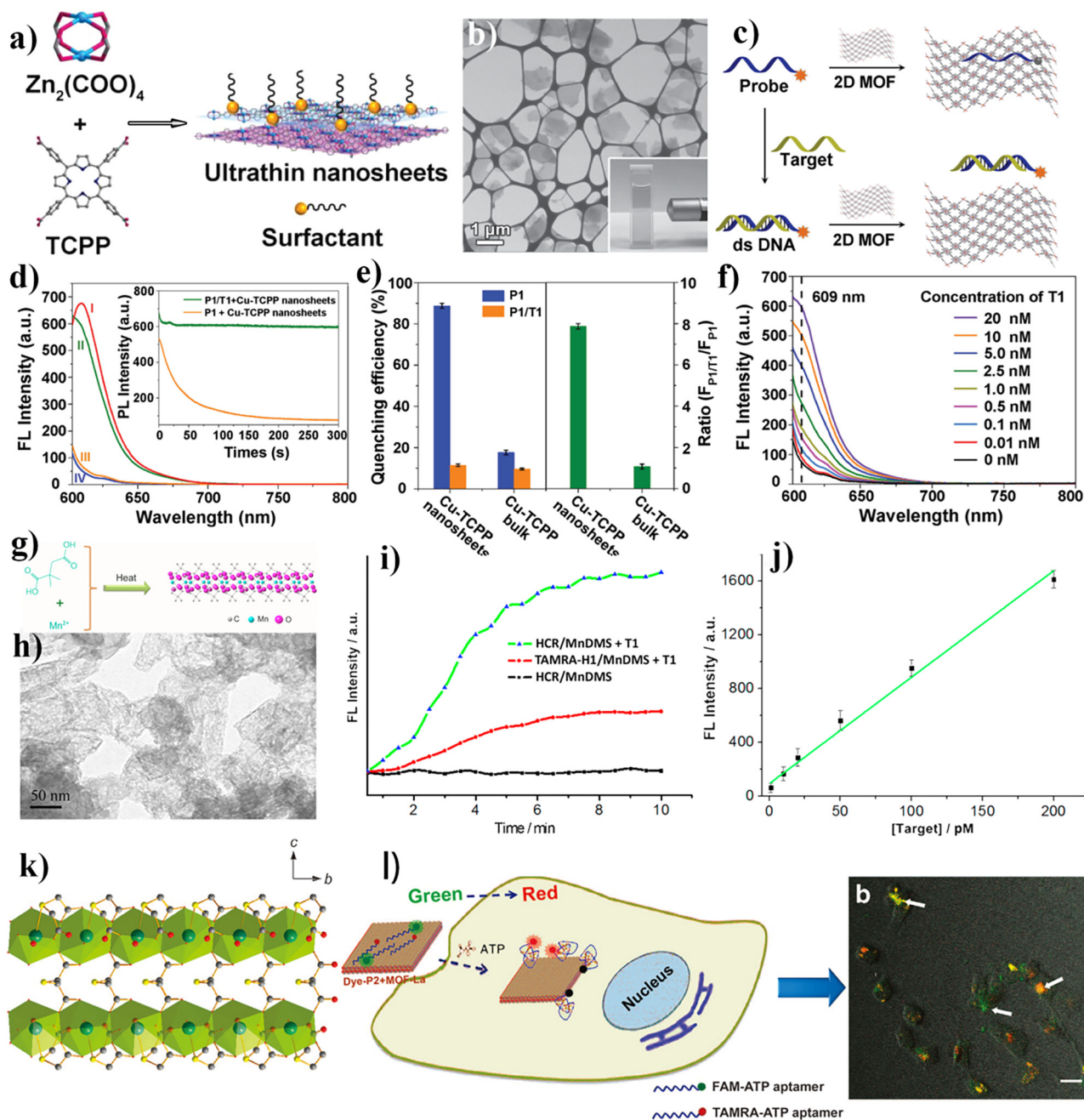


**Fig. 18.** MOF nanosheet for biosensing. (a–f) Zn-TCPP nanosheets used for DNA detection. Copyright © 2015 WILEY-VCH Verlag GmbH & Co. KGaA, Weinheim. (g–j) Synthesis and morphology of MnDMS nanosheets and its (i–j) fluorescent sensing for T1 detection. (k) The structure of MOF-La and (l) schematic illustration of dye-P2 + MOF-La used to detect intracellular adenosine.

facilitated the diffusion of both substrates and product (Fig. 16e–g). Impressively, all thioanisole could be converted into quantitatively corresponding sulfone without the occurrence of any adverse reactions.

Moreover, MOF nanosheets were also applied as carriers-loaded noble metal catalyst, which had demonstrated excellent catalytic properties [120,121]. In 2014, a 2D hierarchical-pore MOF nanosheet with immobilizing Pd nanoparticles (Zn/Ni-MOF-2 NAHNS) was applied to catalyze the CO-based multicomponent alkoxy carbonylation of aryl halides reactions (Fig. 17a–c) [120]. The results indicated that the hollow nanocubes assembled by these Zn/Ni-MOF-2 nanosheets had high specific surface area and more accessible load sites, leading to the uniform distribution of

the immobilized Pd clusters (size: 2.1 nm) onto the nanosheets than the bulk MOFs. Moreover, CO could be easily absorbed in these nanosheets, adding to the probability of contact with active Pd. Therefore, compared with regular supported catalysts palladium (such as Pd black), such hybrid MOF nanosheets with well-distributed Pd clusters had presented superior and more stable catalytic properties. Additionally, almost all substrates were reactive and could yield products as media in high yields within 24 h at 60 °C. Later in 2016, the freestanding Pd-H-MOF-5 nanosheets were obtained by the same research group, which were then used to catalyze the reduction of nitroarenes (Fig. 17d–f) [121]. Similarly, the porosity of MOF-5 was good for H<sub>2</sub> adsorption, and nanosheets with large surface area could facilitate the dispersion

of active Pd nanoparticles. Thus, due to the unique features of MOF nanosheets, these Pd-H-MOF-5 nanosheets had exhibited excellent catalytic performance (>85% conversion) in the catalytic system, which is much better than Pd@bulk MOF-5 (~40% conversion).

It is a favorable strategy to load novel metal particles onto MOF nanosheets as a biomimetic catalyst. In 2017, Zhang and coworkers [122] had reported the peroxidase-like active Au NPs/Cu-TCPP(M) hybrid nanosheets (Fig. 17g, i). Specifically, the cascade reactions mimicking natural enzymes could be successfully achieved, thanks to the multiple functions of catalytic species in these hybrid nanosheets systems. As shown in Fig. 17h, two reactions, namely, oxidation of Glucose and TMB, respectively, could be directly catalyzed by Au NPs/Cu-TCPP(M) hybrid nanosheets, and the oxidized TMB (oxTMB) and gluconic acid were generated simultaneously. Furthermore, these hybrid nanosheets could also be used to detect glucose, which had exhibited good sensing performance (Fig. 17j–k). Such important finding contributes to the design of multifunctional biomimetic catalysts based on the nanomaterials.

### 3.3. Sensing

Given the good capability of molecular recognition luminescence or electrochemical change, MOF nanosheets can also serve as sensors with high sensitivity and selectivity. Therefore, they represent the inspiration for a new generation of sensing system. Here, some examples about sensing of MOF nanosheets are presented. More specifically, DNA detection, luminescent sensing of Fe<sup>3+</sup>, and sensing of ethylamine based on MOF nanosheets will be provided in details.

#### 3.3.1. Biosensing

MOF nanosheets with biocompatibility are frequently applied in the field of biosensor. These sensors possess excellent selectivity, which may potentially be used for real sample analysis. Zhang and coworkers had used M-TCPP nanosheets (M = Co, Cu, Zn, and Cd) as new sensing platforms to detect DNA (Fig. 18a–c) [84]. The general principle was as shown in Fig. 18c. To be specific, the MOF nanosheets could adsorb the dye-labeled ssDNA, resulting in fluorescence quenching of the dye. Contrarily, dsDNA with complementary DNA would weakly interact with MOF nanosheets, thus avoiding fluorescence quenching. For example, the thin Cu-TCPP nanosheets could easily absorb the texas red-labeled ssDNA, thus leading to rapid fluorescence quenching. Typically, 95% quenching efficiency could be achieved within five minutes. However, for dsDNA with target complementary DNA, the fluorescence was barely affected by Cu-TCPP nanosheets. Furthermore, quantitative tests using target DNA to various concentrations were also performed, which exhibited extremely low detection limits ( $20 \times 10^{-12}$  M) and a wide detection range ( $0\text{--}5 \times 10^{-9}$  M) (Fig. 18f). All these results highlighted the advantages of MOF nanosheets, among which, their porosity and accessibility are beneficial to energy transfer and acceleration of fluorescence quenching, apart from the increased surface area for DNA adsorption.

Another fluorescent sensing MOF nanosheet was reported by Song and coworkers [123]. Combined with the hybrid chain reaction methods, Mn(C<sub>6</sub>H<sub>8</sub>O<sub>4</sub>)(H<sub>2</sub>O) nanosheets (Fig. 18g–h) showed a relatively wide linear detection range (1 pM–200 pM) and a lower detection limit (0.2 pM) (Fig. 18i–j). This MOF nanosheets-based fluorescence sensing platform also provided an effective detection method for living cells. For example, in 2017, Xia had used the lanthanide-based MOF nanosheets as the bioanalytical platforms and achieved the two-color living cell imaging of intracellular adenosine (Fig. 18k–l) [28]. Noteworthy, the molecular ratio of FAM-aptamer loaded on dye-aptamer/MOF-Ln nanosheets to TAMRA-aptamer could be adjusted, which could further achieve the intracellular detection of small molecules and DNA. Moreover,

the target intracellular ATP was also successfully applied in this system.

#### 3.3.2. Optochemical sensor

MOF nanosheets can also serve as a versatile platform of optochemical sensor due to their capabilities of fluorescence and molecular recognition luminescence. In 2008, Jiang had synthesized [Zn(BDC)(H<sub>2</sub>O)]<sub>n</sub> sheets with fluorescence property, which could sensitively and quantitatively detect ethylamine by changing the fluorescence emission intensity and increasing the ethylamine concentration [124] (Fig. 19a–c). In 2016, Qian had fabricated a luminescent MOF Ti<sub>2</sub>(HDOBDC)<sub>2</sub>(H<sub>2</sub>DO-BDC) nanosheet, which had a fast response to Fe<sup>3+</sup> ions with high sensitivity (Fig. 19d–f) [42]. Compared with the slow response (usually several hours to one day) of bulky MOFs with unique pore structure and ability to quickly identify compounds, fluorescence quenching of the 2D NTU-9-NS nanosheets only takes 10 s after the addition of Fe<sup>3+</sup>, thanks primarily to the high dispersion of the nanosheets and the easy access to the active center on the surface. Besides, the ppm levels of Fe<sup>3+</sup> ions could efficiently quench the fluorescence of nanosheets in aqueous solution, which also exerted the quantitative luminescent quenching effect at different pH levels. In 2017, Tan had presented a tunable optochemical platform based on MOF {(HN(Et<sub>3</sub>)<sub>2</sub>[Zn<sub>3</sub>BDC<sub>4</sub>]-solvent {solvent = DMF or DMA} nanosheets for the sensing of various small molecules (Fig. 19g–i) [125]. Typically, these nanosheets could absorb the small light-emitting molecules. Considering the strong host–guest coupling effect, these functionalized guest@MOF porous nanosheets could integrate the unusual optical properties. Therefore, such “guest@host” composite system with tunable luminescent properties can serve as a platform for photonics-based chemical sensing.

#### 3.3.3. Electrochemical sensing

MOF nanosheets are also used in the electrochemical sensing platform to detect water, H<sub>2</sub>O<sub>2</sub> and cocaine, as a result of their electrochemical activity. In 2016, Zhang and coworkers had utilized the ultrathin M-TCPP(Fe) nanosheets (M = Zn, Cu, and Co) for the quantitative detection of H<sub>2</sub>O<sub>2</sub> [85] (Fig. 20a–c). GC/M-TCPP(Fe) nanosheets, which were assembled onto electrodes, manifested typical amperometric response to H<sub>2</sub>O<sub>2</sub>, with a fairly low detection limit. More importantly, the electrodes assembled with Co-TCPP(Fe) nanosheets were featured by their wide linear dynamic range ( $0.4 \times 10^{-6}$ – $50 \times 10^6$  M), high catalytic selectivity toward H<sub>2</sub>O<sub>2</sub>, high reproducibility and excellent long-term storage stability (at least five weeks). Moreover, they could also realize the real-time monitoring of H<sub>2</sub>O<sub>2</sub> in living cells, which was thereby promising for detecting breast cancer.

In the same year, Yao had reported Cu<sub>3</sub>TCPP nanosheets, which had displayed excellent capacitance and humidity-sensing properties (Fig. 20d–f) [126]. Although the pores of the MOF itself are hydrophobic, the MOF nanosheets have better proton conductivity due to the tremendous –COOH functional groups suspended around the outside of the nanosheets. After being pressed into a pellet, the Cu<sub>3</sub>TCPP nanosheets showed a distinct capacitance-frequency characteristic under different relative humidity (RH) and exhibited the high capacitance response as well as sensitivity at 1 kHz. Astonishingly, they had also demonstrated obvious response peak from 60% to 98% RH, along with good reversibility and reproducibility through exposure/recovery cycles from low to high RH. In 2017, Du and co-workers [127] had prepared the Au nanocluster-embedded zirconium-based MOF nanosheet composites (AuNCs@521-MOF), which was applied as an electrochemical aptasensor for detecting cocaine (Fig. 20g–i). Typically, the cocaine aptamer strands immobilized AuNCs@521-MOF nanosheet possessed excellent bioaffinity and electrochemical activity, which could thereby form a biosensitive platform for detecting cocaine.

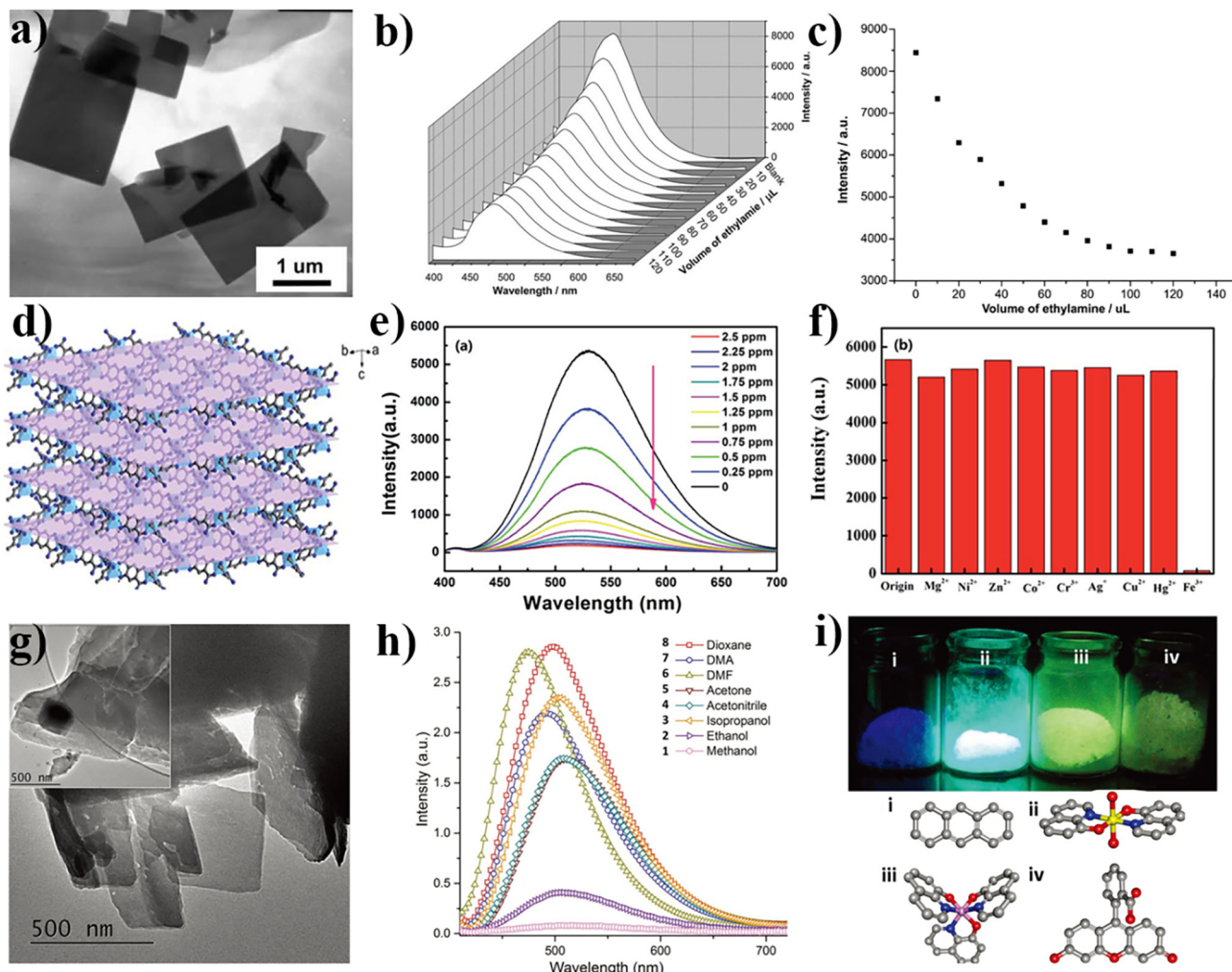


**Fig. 19.** MOF nanosheets for photonics-based chemical sensing. (a–c)  $[\text{Zn}(\text{BDC})(\text{H}_2\text{O})]_n$  nanosheets and the fluorescence sensor of ethylamine; (d–f) Structure and the specific metal ions selectivity of NTU-9-NS. Copyright © 2016, Royal Society of Chemistry. (g–i) Optochemical behavior of  $\text{ZnQDMF@OX-1}$  nanosheets and the luminous optics of different luminescent guest molecules adsorbed by OX-1. Copyright © 2017 WILEY-VCH Verlag GmbH & Co. KGaA, Weinheim.

This aptasensor could detect cocaine sensitivity; meanwhile, it exhibited a wide detection range ( $0.001\text{--}1.0\text{ ng}\cdot\text{mL}^{-1}$ ), a low detection limit ( $0.44\text{ pg}\cdot\text{mL}^{-1}$ ) and specific selectivity. Thus, MOF nanosheets still have a bright future in the field of electrochemical sensors, regardless of the limitation in the conductivity of MOFs.

### 3.4. Energy storage and transfer

MOF nanosheets with high surface area and porosity are the popular electrode materials, which are suitable for energy storage and transfer, especially in the field of supercapacitors [128]. In 2016, Chen [43] had reported applying the layered  $[\text{Ni}_3(\text{OH})_2(\text{C}_8\text{H}_4\text{O}_4)_2(\text{H}_2\text{O})_4]\cdot 2\text{H}_2\text{O}$  nanosheets (Ni-MOF) in the alkaline battery-supercapacitor hybrid devices (ABSHD) (Fig. 21a–c). These 2D-layered Ni-MOF nanosheets possessed a unique 1D-chain crystal structure in each layer, which was beneficial for electron conduction. Moreover, the interspaces between layers in nanosheets could also promote the diffusion and storage of electrolyte ions. Thus, a high specific capacity was demonstrated in the KOH electrolyte, with Ni-MOF nanosheets being used as the working electrodes. The energy storage could be further improved in the mixed electrolyte containing  $\text{K}_4\text{Fe}(\text{CN})_6$ , since  $\text{Fe}(\text{CN})_6^{4-}/\text{Fe}(\text{CN})_6^{3-}$  could couple with Ni(II)/Ni(III) and could thereby be stored

and diffused in the interspaces within the 2D-layered Ni-MOFs which is better than the bulk Ni-MOF. Using carbon nanotubes decorated with carboxylic acid (CNTs-COOH) as the negative electrodes, the ABSHD had exhibited increased supercapacitor performance, together with a high-power density ( $7000\text{ W Kg}^{-1}$ ), a high energy density ( $55.8\text{ W h kg}^{-1}$ ) and a large voltage window ( $1.4\text{ V}$ ). Subsequently, in 2017, this Ni-MOF was transformed to a mixed-metallic MOF (M-MOF) through partially substituting  $\text{Ni}^{2+}$  with  $\text{Co}^{2+}$  or  $\text{Zn}^{2+}$ , which was thus used as the positive electrode material in supercapacitor (Fig. 21d–f) [44]. The  $[\text{Ni}_{3-x}\text{Co}_x(\text{OH})_2(\text{tp})_2(\text{H}_2\text{O})_4]\cdot 2\text{H}_2\text{O}$  ( $x \approx 0.69$ ) (Co/Ni-MOF) nanosheet had presented an enhanced conductivity by doping  $\text{Co}^{2+}$ . Thus, improved capacity could be achieved when it was assembled into the hybrid supercapacitors, along with a high energy density ( $49.5\text{ W h kg}^{-1}$ ) and an excellent power density ( $1450\text{ W kg}^{-1}$ ). Moreover, Wei [45] had reported a layered structural Co-MOF ( $\text{Co}_2(\text{OH})_2\text{C}_8\text{H}_4\text{O}_4$ ) nanosheets with conductive network frames (Co-O-Co chain), which was beneficial for improving its electrochemical performance (Fig. 21g–i). Notably, the supercapacitor, whose working electrode was mixed with 80 wt% of Co-MOF nanosheets, had exhibited typical pseudocapacitive performance with good stability and rate capability. Furthermore, the supercapacitor could reach a high specific capacitance of  $2564\text{ F g}^{-1}$ . All of the above examples have demonstrated the advantages of this

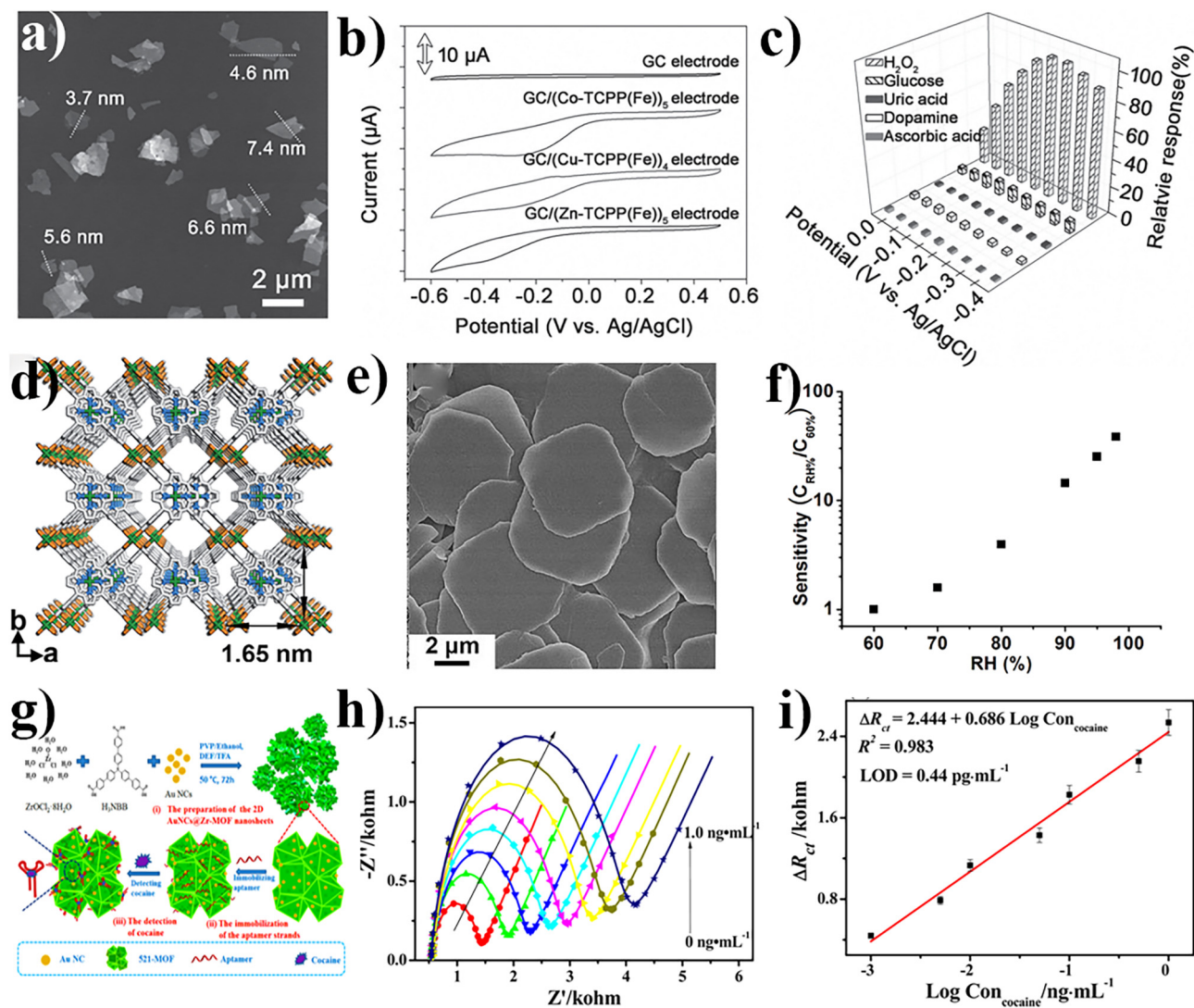


**Fig. 20.** MOF nanosheets for electrochemical sensing. (a) The morphology and thickness of the MOF nanosheets; (b) The CV curves of electrodes decorated with M-TCPP(Fe) nanosheets; (c) The amperometric responses to different analytes. Copyright © 2016 WILEY-VCH Verlag GmbH & Co. KGaA, Weinheim. (d–f) Structure, morphology and RH dependent sensitivity of  $\text{Cu}_3\text{TCPP}$ . Copyright © 2016, Royal Society of Chemistry. (g–i) AuNCs@Zr-MOF nanosheets based electrochemical biosensing were used to detect various amounts of cocaine. Copyright © 2017, American Chemical Society.

strategy for supercapacitors, and an increasing number of MOF nanosheets are suggested to be used in the energy field in the near future.

In addition, MOF nanosheets can also be used in photoelectric conversion. For instance, in 2016, Zhang [129] fabricated a photoelectrochemical cell, with  $\text{CuS}/\text{M-TCPP}$  ( $\text{M} = \text{Co}, \text{Cu}, \text{or Cd}$ ) composite nanosheets being used as the active materials, and such cell had presented excellent photoelectrochemical performance. What's more, MOF nanosheets were also compared with photosensitive 3D MOFs, so as to investigate the influence of dimensions on resonance energy transfer. Recently in 2017, Lin and coworkers had prepared MOF nanosheet (2D-MOLs) and 3D-MOF, respectively, using the same ligands and similar SBUs. In this system, the ligand acted as a light-harvesting chromophore, which displayed different energy transfer performances under different dimensions (Fig. 22) [130]. Such ligand was associated with a low linkability and slow exciton migration, which resulted in the low transfer efficiency of MOF nanosheets. Nonetheless, the confinement effect of nanosheets has facilitated the transition dipole alignment; consequently, MOF nanosheets allow for energy transfer in a faster

and more efficient way. Taken together, MOF nanosheets are superb candidates for light capture and energy transfer.

### 3.5. Enzyme inhibitor

MOF nanosheets, which are characterized by their large surface areas, good dispersibility, abundant surface charge and organic ingredients, are suitable for protein binding, making it easier to understand the interface chemistry between enzymes and MOF. Without using relatively large sized bulk crystals of MOFs with inhomogeneous dispersion in water, Zhou had prepared  $\text{Zn}_2(\text{bim})_4$  and  $\text{Cu}(\text{bpy})_2(\text{OTf})_2$  nanosheets with good dispersibility and large surface areas to investigate the modulation effect of enzyme activity [131]. (Fig. 23) Compared with the  $\text{Zn}_2(\text{bim})_4$  nanosheets that showed no obvious inhibition on  $\alpha$ -chymotrypsin (ChT), the  $\text{Cu}(\text{bpy})_2(\text{OTf})_2$  nanosheets had displayed excellent inhibition (96.9%) due to the role of Cu(II) center in nanosheets. In this system, effective contact between the substrate and the active site in enzyme is activated by the irreversible interaction of Cu(II) with



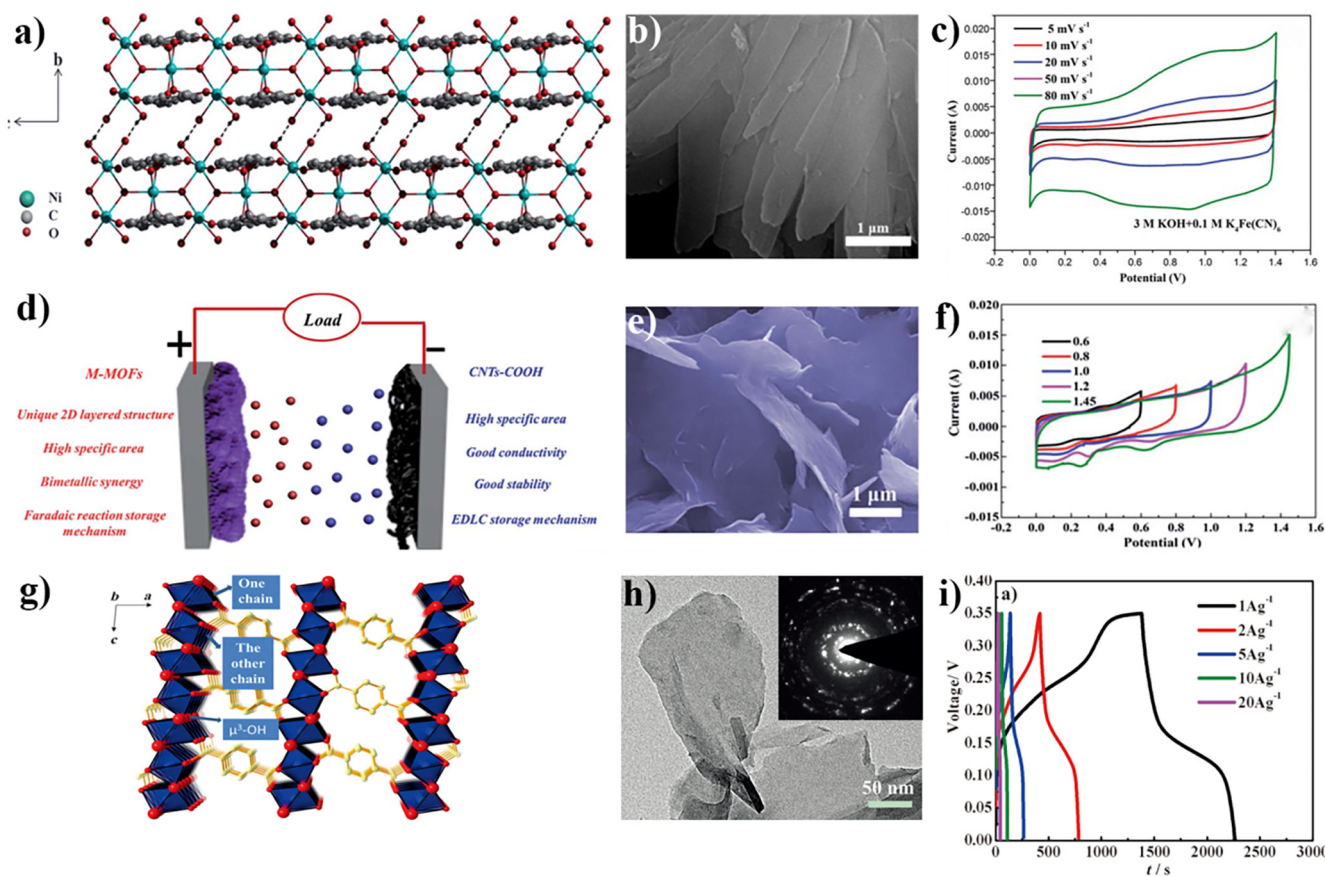


**Fig. 21.** Supercapacitors based on MOF nanosheets. (a) Structure and (b) morphology of Ni-MOF; (c) CV curves of supercapacitor based on Ni-MOF//CNTs-COOH ABSHD. Copyright © 2016, Royal Society of Chemistry. (e) Morphology of Co/Ni-MOF, (d) Illustration and (f) CV curves of hybrid supercapacitors based on Co/Ni-MOF and CNTs-COOHs. Copyright © 2016, Royal Society of Chemistry. (g) Structure and morphology of the Co-MOF; (i) Charge-discharge profiles of the Co-MOF based supercapacitor. Copyright © 2017 Wiley-VCH Verlag GmbH & Co. KGaA, Weinheim.

His-57, as well as the electrostatic interaction between enzymes and nanosheets.

#### 4. Conclusion and prospects

MOF nanosheets are the emerging and promising nanomaterials during the past few years, which have been applied in extremely important fields, such as catalysis, gas separation, sensors and energy conversion/storage applications. As described previously, the different preparation methods of the recently reported MOF nanosheets have been reviewed in this article. Moreover, the latest developments of the MOF nanosheets-related applications are also discussed, including gas separation; DNA detection; novel catalysis for OER, HER and organic reaction; ultrasensitive molecular sensors; energy storage and transfer; and enzyme inhibitor.

In the meantime, the potential challenges and possible research directions are also described for the better and deeper utilization of MOF nanosheet materials. Nevertheless, there is still a long way to go to achieve scalable and controllable preparation of the molecular-scale nanosheets both in solution systems and on substrates. The following problems should arouse out attention. 1) Thickness of the obtained MOF nanosheets is not uniform, and it is still difficult for the controllable preparation of monolayer in a high yield. 2) Most prepared MOF nanosheets have the lateral sizes of less than micrometer; particularly, the monolayer MOF nanosheets have smaller area (hundred nm), numerous defects, and irregular shapes, which have added to the difficulties in device

processing and severely inhibited their applications in fields such as optics, electrics and magnetics. 3) All existing preparation methods would cause chemical/physical damage to MOF nanosheets, giving rise to deviated structures and properties from the ideal ones. 4) The prepared MOF nanosheets have relative bad crystallinity, especially for the samples obtained through the bottom-up methods, which has hampered the determination of their structure information to reveal the structure-performance relationship. 5) MOF nanosheets with different structure orientations may present different apertures on their basal planes, which may induce remarkably distinct performances. Hence, it remains a huge challenge to prepare MOF nanosheets in different orientations. In addition, most MOF nanosheets have insufficient conductivity and poor stability, which have thereby limited their applications in the field of energy conversion and storage.

Apart from the unknown mechanism of action in the applications, MOF nanosheets are relatively fragile. They are sensitive to heat, light, and electron beams. Therefore, the support of novel in-situ characterization techniques is required for the application of MOF nanosheets, so that its specific role can be further understood.

Moreover, high quality and continuous film with few defects are needed to prepare these devices (especially electrical device). For example, the modular assembly, hot-drop, spin coating and in-situ growth methods have been used to prepare MOF nanosheet films in a fast assembly process. However, in most cases, the films are associated with numerous defects and random orientation. Therefore, new film preparation methods using MOF nanosheets

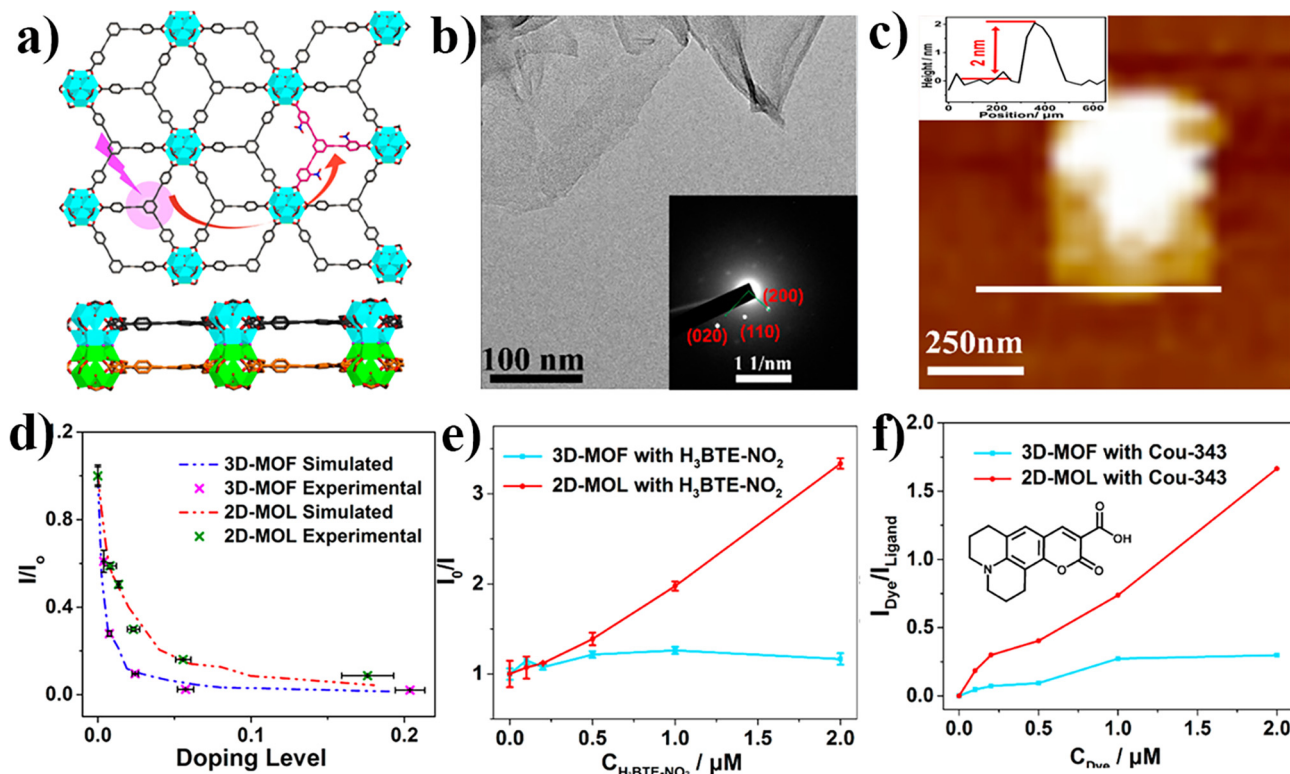


Fig. 22. MOF nanosheets used for photoelectric conversion. (a) Structure and (b, c) morphology of 2D-MOL; (d) Intensity quenching of 2D-MOLs and 3D-MOFs; (e, f)  $I_{\text{Dye}}/I_{\text{Ligand}}$  and  $I_0/I$  curves of fluorescence quenching about 3D-MOF and 2D-MOL. Copyright © 2017, American Chemical Society.

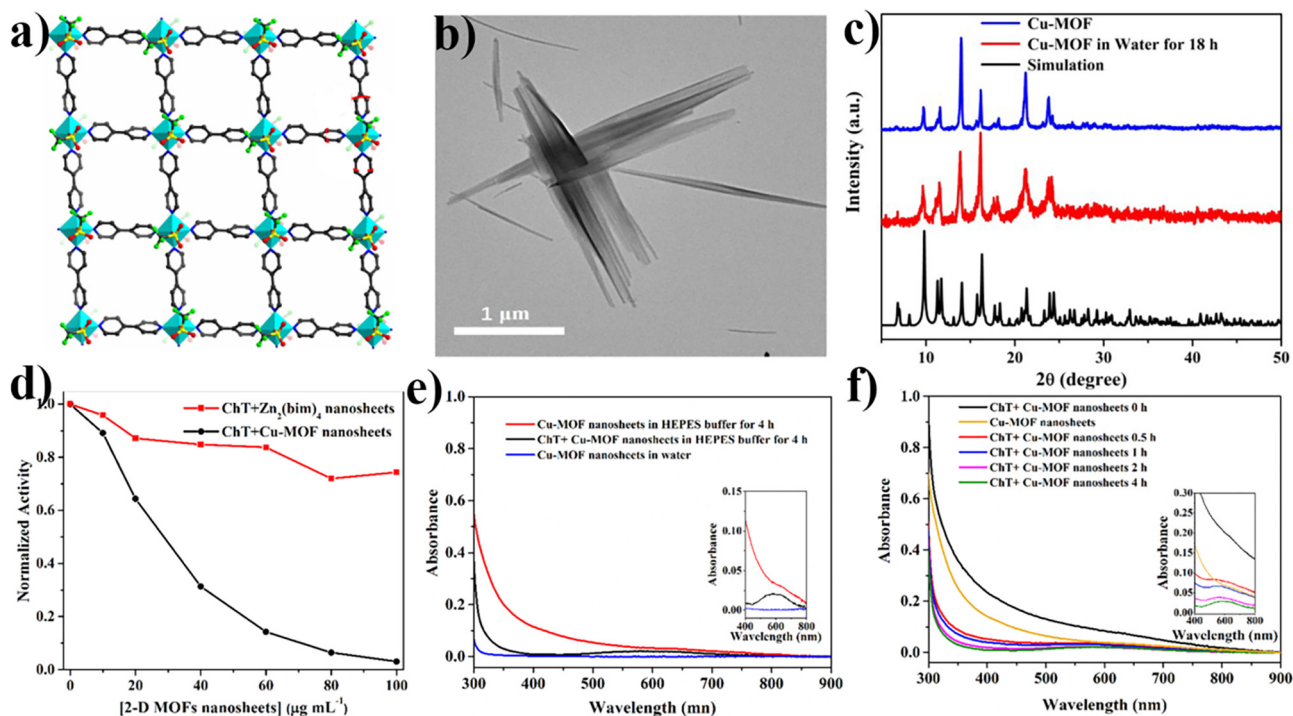


Fig. 23. Modulation effect of MOF nanosheets with enzyme activity. (a) Structure, (b) Morphology and (c) XRD patterns of Cu-MOF; (d) The activity of ChT with 2-D Cu-MOF and  $\text{Zn}_2(\text{bim})_4$  nanosheets. UV absorbance of (e) 2-D Cu-MOF nanosheets and (f) 2-D Cu-MOF nanosheets ( $200 \mu\text{g mL}^{-1}$ ) incubated with ChT. Copyright © 2017, American Chemical Society.

are desired. Furthermore, the multifunctional inorganic nanosheets can be grown through grafting two functional structures in the same nanosheet. From the perspective of coordination

chemistry, the multifunctional MOF nanosheets can be prepared in a simpler way through the strategies like mixing ligands and mixed metals.

After all, the purposeful and rational design and the preparation of MOF nanosheets with specific structure and performance remain in its infancy. Compared with the tens of thousands of bulk MOF structures, only a few of them have been successfully prepared to nanosheets. As a result, more practical new MOF nanosheet materials will be exploited by taking full advantage of both the unique properties of MOF and the features of nanosheets. Additionally, new methods and chemicals to massively produce MOF nanosheets with good crystallinity, large lateral size and uniformly controlled thickness are urgently desired. A series of issues have not sufficiently discussed so far, but they are promising to be solved in the near future with more researchers participating in this field of study. Undeniably, MOF nanosheets show great potentials in specific applications, and increasing attention should be paid to this promising field of research.

## Acknowledgements

This work was supported by National Key R&D Program of China (2017YFA0206802), Key Research Program of Frontier Science, CAS (QYZDB-SSW-SLH023), the National Natural Science Foundation of China, China (21773245, 21401193), the Strategic Priority Research Program of CAS (XDB20000000), Scientific Research and Equipment Development Project, CAS (YZ201609), and the Natural Science Foundation of Fujian Province (2016J06006, 2015J01230, 2016J05053, 2017J05034).

## References

- G. Lu, S.Z. Li, Z. Guo, O.K. Farha, B.G. Hauser, X.Y. Qi, Y. Wang, X. Wang, S.Y. Han, X.G. Liu, J.S. DuChene, H. Zhang, Q.C. Zhang, X.D. Chen, J. Ma, S.C.J. Loo, W.D. Wei, Y.H. Yang, J.T. Hupp, F.W. Huo, *Nature Chem.* 4 (2012) 310–316.
- S. Li, X. Liu, H. Chai, Y. Huang, *TrAC, Trends Anal. Chem.* 105 (2018) 391–403.
- X. Liu, B. Tang, J. Long, W. Zhang, X. Liu, Z. Mirza, *Sci. Bull.* 63 (2018) 502–524.
- W. Zhang, Z. Wu, H. Jiang, S. Yu, *J. Am. Chem. Soc.* 136 (2014) 14385–14388.
- M. Jahan, Q.L. Bao, J.X. Yang, K.P. Loh, *J. Am. Chem. Soc.* 132 (2010) 14487–14495.
- M.S. Yao, W.X. Tang, G.E. Wang, B. Nath, G. Xu, *Adv. Mater.* 28 (2016) 5229–5234.
- W.H. Li, K. Ding, H.R. Tian, M.S. Yao, B. Nath, W.H. Deng, Y.B. Wang, G. Xu, *Adv. Fun. Mater.* 27 (2017) 1702067.
- C. Huxford, J. Della Rocca, W.B. Lin, *Curr. Opin. Chem. Biol.* 14 (2010) 262–268.
- S. Sorribas, P. Gorgojo, C. Tellez, J. Coronas, A.G. Livingston, *J. Am. Chem. Soc.* 135 (2013) 15201–15208.
- S. Li, Y. Chen, X. Pei, S. Zhang, X. Feng, J. Zhou, B. Wang, *Chin. J. Chem.* 34 (2016) 175–185.
- M. Xu, T. Liang, M. Shi, H. Chen, *Chem. Rev.* 113 (2013) 3766–3798.
- P.Z. Li, Y. Maeda, Q. Xu, *Chem. Commun.* 47 (2011) 8436–8438.
- P. Amo-Ochoa, L. Welte, R. González-Prieto, P.J. SanzMiguel, C.J. Gómez-García, E. Mateo-Martí, S. Delgado, J. Gómez-Herrero, F. Zamora, *Chem. Commun.* 46 (2010) 3262–3264.
- C. Hermosa, B.R. Horrocks, J.I. Martínez, F. Liscio, J. Gomez-Herrero, F. Zamora, *Chem. Sci.* 6 (2015) 2553–2558.
- C. Martí-Gastaldó, J.E. Warren, K.C. Stylianou, N.L.O. Flack, M.J. Rosseinsky, *Angew. Chem. Int. Ed.* 51 (2012) 11044–11048.
- A. Kondo, C.C. Tiew, F. Moriguchi, K. Maeda, *Dalton Trans.* 42 (2013) 15267–15270.
- J.C. Tan, P.J. Saines, E.G. Bithell, A.K. Cheetham, *ACS Nano* 6 (2012) 615–621.
- P.J. Beldon, S. Tominaka, P. Singh, T. Saha Dasgupta, E.G. Bithell, A.K. Cheetham, *Chem. Commun.* 50 (2014) 3955–3957.
- P.J. Saines, J.C. Tan, H.H.-M. Yeung, P.T. Bartonb, A.K. Cheetham, *Dalton Trans.* 41 (2012) 8585–8593.
- P.J. Saines, M. Steinmann, J.C. Tan, H.H.M. Yeung, W. Li, P.T. Barton, A.K. Cheetham, *Inorg. Chem.* 51 (2012) 11198–11209.
- J.A. Foster, S. Henke, A. Schneemann, R.A. Fischer, A.K. Cheetham, *Chem. Commun.* 52 (2016) 10474–10477.
- T. Araki, A. Kondo, K. Maeda, *Chem. Commun.* 49 (2013) 552–554.
- Y. Peng, Y. Li, Y. Ban, H. Jin, W. Jiao, X. Liu, W. Yang, *Science* 346 (2014) 1356–1359.
- G.E. Gomez, M.C. Bernini, E.V. Brusau, G.E. Narda, D. Vega, A.M. Kaczmarek, R. Van Deun, M. Nazzarro, *Dalton Trans.* 44 (2015) 3417–3429.
- G. Lamming, O. El-Zubir, J. Kolokotroni, C. McGurk, P.G. Waddell, M.R. Probert, A. Houlton, *Inorg. Chem.* 55 (2016) 9644–9652.
- P. Chandrasekhar, A. Mukhopadhyay, G. Savitha, J.N. Moorthy, *J. Mater. Chem. A* 5 (2017) 5402–5413.
- M.J. Cliffe, E. Castillo-Martínez, Y. Wu, J. Lee, A.C. Forse, F.C.N. Firth, P.Z. Moghadam, D. Fairen-Jimenez, M.W. Gaultois, J.A. Hill, O.V. Magdysyuk, B. Slater, A.L. Goodwin, G.P. Grey, *J. Am. Chem. Soc.* 139 (2017) 5397–5404.
- H.S. Wang, J. Li, J.Y. Li, K. Wang, Y. Ding, X.H. Xia, *NPG Asia Mater.* 9 (2017), <https://doi.org/10.1038/am.2017.7> e354.
- Y. Ding, Y.P. Chen, X. Zhang, L. Chen, Z. Dong, H.L. Jiang, H. Xu, H.C. Zhou, *J. Am. Chem. Soc.* 139 (2017) 9136–9139.
- T. Kambe, R. Sakamoto, K. Hoshiko, K. Takada, M. Miyachi, J.H. Ryu, S. Sasaki, J. Kim, K. Nakazato, M. Takata, H. Nishihara, *J. Am. Chem. Soc.* 135 (2013) 2462–2465.
- X. Sun, K.H. Wu, R. Sakamoto, T. Kusamoto, H. Maeda, X. Ni, W. Jiang, F. Liu, S. Sasaki, H. Masunaga, H. Nishihara, *Chem. Sci.* 8 (2017) 8078–8085.
- T. Tsukamoto, K. Takada, R. Sakamoto, R. Matsuoka, R. Toyoda, H. Maeda, T. Yagi, M. Nishikawa, N. Shinjo, S. Amano, T. Iokawa, N. Ishibashi, T. Oi, K. Kanayama, R. Kinugawa, Y. Koda, T. Komura, S. Nakajima, R. Fukuyama, N. Fuse, M. Mizui, M. Miyasaki, Y. Yamashita, K. Yamada, W. Zhang, R. Han, W. Liu, T. Tsubomura, H. Nishihara, *J. Am. Chem. Soc.* 139 (2017) 5359–5366.
- K. Takada, R. Sakamoto, S.T. Yi, S. Katagiri, T. Kambe, H. Nishihara, *J. Am. Chem. Soc.* 137 (2015) 4681–4689.
- R. Sakamoto, T. Yagi, K. Hoshiko, S. Kusaka, R. Matsuoka, H. Maeda, Z. Liu, Q. Liu, W.Y. Wong, H. Nishihara, *Angew. Chem. Int. Ed.* 56 (2017) 3526–3530.
- R. Sakamoto, K. Hoshiko, Q. Liu, T. Yagi, T. Nagayama, S. Kusaka, M. Tsuchiya, Y. Kitagawa, W.-Y. Wong, H. Nishihara, *Nat. Commun.* 6 (2015) 6713–6716.
- T. Rodenas, I. Luz, G. Prieto, B. Seoane, H. Miro, A. Corma, F. Kapteijn, F.X.L. i Xamena, J. Gascon, *Nature Mater.* 14 (2015) 48–55.
- Y. Peng, Y. Li, Y. Ban, W. Yang, *Angew. Chem. Int. Ed.* 56 (2017) 9757–9761.
- H. Ang, L. Hong, A.C.S. Appl. Mater. Interfaces 9 (2017) 28079–28088.
- L. Cao, Z. Lin, F. Peng, W. Wang, R. Huang, C. Wang, J. Yan, J. Liang, Z. Zhang, T. Zhang, L. Long, J. Sun, W. Lin, *Angew. Chem. Int. Ed.* 55 (2016) 4962–4966.
- R. Dong, M. Pfeffermann, H. Liang, Z. Zheng, X. Zhu, J. Zhang, X. Feng, *Angew. Chem. Int. Ed.* 54 (2015) 12058–12063.
- S. Zhao, Y. Wang, J. Dong, C.T. He, H. Yin, P. An, K. Zhao, X. Zhang, C. Gao, L. Zhang, J. Lv, J. Wang, J. Zhang, A.M. Khattak, N.A. Khan, Z. Wei, J. Zhang, S. Liu, H. Zhao, Z. Tang, *Nature Energy* 1 (2016) 16184.
- H. Xu, J. Gao, X. Qian, J. Wang, H. He, Y. Cui, Y. Yang, Z. Wang, G. Qian, *J. Mater. Chem. A* 4 (2016) 10900–10905.
- Y. Jiao, J. Pei, C. Yan, D. Chen, Y. Hu, G. Chen, *J. Mater. Chem. A* 4 (2016) 13344–13351.
- Y. Jiao, J. Pei, D. Chen, C. Yan, Y. Hu, Q. Zhang, G. Chen, *J. Mater. Chem. A* 5 (2017) 1094–1102.
- J. Yang, Z. Ma, W. Gao, M. Wei, *Chem. Eur. J.* 23 (2017) 631–636.
- D. Rodriguez-San-Miguel, P. Amo-Ochoa, F. Zamora, *Chem. Commun.* 52 (2016) 4113–4127.
- G. Liu, W. Jin, N. Xu, *Angew. Chem. Int. Ed.* 55 (2016) 13384–13397.
- R. Sakamoto, K. Takada, T. Pal, H. Maeda, T. Kambe, H. Nishihara, *Chem. Commun.* 53 (2017) 5781–5801.
- M.T. Zhao, Q.P. Lu, Q.L. Ma, H. Zhang, *Small Methods* 1 (2017) 1600030.
- M. Zhao, Y. Huang, Y. Peng, Z. Huang, Q. Ma, H. Zhang, *Chem. Soc. Rev.* 47 (2018) 6267–6295.
- X. Cao, C. Tan, M. Sindoro, H. Zhang, *Chem. Soc. Rev.* 46 (2017) 2660–2677.
- S. Furukawa, J. Reboul, S. Diring, K. Sumida, S. Kitagawa, *Chem. Soc. Rev.* 43 (2014) 5700–5734.
- M. Sindoro, N. Yanai, A.-Y. Jee, S. Granick, *Acc. Chem. Res.* 47 (2014) 459–469.
- A. Carne, C. Carbonell, I. Imaz, D. Maspoch, *Chem. Soc. Rev.* 40 (2011) 291–305.
- Y. Li, J. Tang, L. He, Y. Liu, Y. Liu, C. Chen, Z. Tang, *Adv. Mater.* 27 (2015) 4075–4080.
- J. Della Rocca, D.M. Liu, W.B. Lin, *Acc. Chem. Res.* 44 (2011) 957–968.
- R. Xu, Y. Wang, X. Duan, K. Lu, D. Micheroni, A. Hu, W. Lin, *J. Am. Chem. Soc.* 138 (2016) 2158–2161.
- K.S. Novoselov, D. Jiang, F. Schedin, T.J. Booth, V.V. Khotkevich, S.V. Morozov, A.K. Geim, *Proc. Natl. Acad. Sci. U. S. A.* 102 (2005) 10451–10453.
- M. Yi, Z. Shen, *J. Mater. Chem. A* 3 (2015) 11700–11715.
- H. Li, J. Wu, Z.Y. Yin, H. Zhang, *Acc. Chem. Res.* 47 (2014) 1067–1075.
- A. Abherve, S. Mañas-Valero, M. Clemente-León, E. Coronado, *Chem. Sci.* 6 (2015) 4665–4673.
- V. Nicolosi, M. Chhowalla, M.G. Kanatzidis, M.S. Strano, J.N. Coleman, *Science* 340 (2013) 1226419.
- Y. Hernandez, V. Nicolosi, M. Lotya, F.M. Blighe, Z. Sun, S. De, I.T. McGovern, B. Holland, M. Byrne, Y.K. Gun'ko, *Nat. Nanotechnol.* 3 (2008) 563–568.
- J.N. Coleman, M. Lotya, A. O'Neill, S.D. Bergin, P.J. King, U. Khan, K. Young, A. Gaucher, S. De, R.J. Smith, *Science* 331 (2011) 568–571.
- Y. Lin, T.V. Williams, J.W. Connell, *J. Phys. Chem. Lett.* 1 (2010) 277–283.
- U. Khan, P. May, A. O'Neill, A.P. Bell, E. Boussac, A. Martin, J. Sempile, J.N. Coleman, *Nanoscale* 5 (2013) 581–587.
- D. Hanlon, C. Backes, T.M. Higgins, M. Hughes, A. O'Neill, P. King, N. McEvoy, G.S. Duesberg, B.M. Sanchez, H. Pettersson, V. Nicolosi, et al., *Chem. Mater.* 26 (2014) 1751–1763.
- J.R. Brent, N. Savjani, E.A. Lewis, S.J. Haigh, D.J. Lewis, P. O'Brien, *Chem. Commun.* 50 (2014) 13338–13341.
- A. Gallego, C. Hermosa, O. Castillo, I. Berlanga, C.J. Gómez-García, E. Mateo-Martí, J.I. Martínez, F. Flores, C. Gómez-Navarro, J. Gómez-Herrero, S. Delgado, F. Zamora, *Adv. Mater.* 25 (2013) 2141–2146.
- P. Joensen, R.F. Frindt, S.R. Morrison, *Mater. Res. Bull.* 21 (1986) 457–461.
- J. Guo, Y. Zhang, Y. Zhu, C. Long, M. Zhao, M. He, X. Zhang, J. Lv, B. Han, Z. Tang, *Angew. Chem. Int. Ed.* 57 (2018) 6873–6877.

- [72] R.A. Laudise, *Prog. Inorg. Chem.* 3 (1962) 1–47.
- [73] A. Rabenau, *Angew. Chem., Int. Ed.* 24 (1985) 1026–1040.
- [74] M.S. Whittingham, *Curr. Opin. Solid. State. Mater. Sci* 1 (1996) 227–232.
- [75] P.J. Hagrman, D. Hagrman, J. Zubietua, *Angew. Chem., Int. Ed.* 38 (1999) 2638–2684.
- [76] J. Gopalakrishnan, *Chem. Mater.* 7 (1995) 1265–1275.
- [77] D. Hagrman, C. Sangregorio, C.J. O'Connor, J. Zubieta, *J. Chem. Soc., Dalton Trans.* (1998) 3707–3709.
- [78] H. Jin, Y. Qi, E. Wang, Y. Li, C. Qin, X. Wang, S. Chang, *Eur. J. Inorg. Chem.* 22 (2006) 4541–4545.
- [79] J.W. Zhao, H.P. Jia, J. Zhang, S.T. Zheng, G.Y. Yang, *Chem.–Eur. J.* 13 (2007) 10030–10045.
- [80] Y. Wang, L. Li, L. Yan, X. Gu, P. Dai, D. Liu, J.G. Bell, G. Zhao, X. Zhao, K.M. Thomas, *Chem. Mater.* 30 (2018) 3048–3059.
- [81] T. He, B. Ni, S. Zhang, Y. Gong, H. Wang, L. Gu, J. Zhuang, W. Hu, X. Wang, *Small* 14 (2018) 1703929.
- [82] G. Xu, T. Yamada, K. Otsubo, S. Sakaida, H. Kitagawa, *J. Am. Chem. Soc.* 134 (2012) 16524–16527.
- [83] S.C. Junggeburth, L. Diehl, S. Werner, V. Duppel, W. Sigle, B.V. Lotsch, *J. Am. Chem. Soc.* 135 (2013) 6157–6164.
- [84] M. Zhao, Y. Wang, Q. Ma, Y. Huang, X. Zhang, J. Ping, Z. Zhang, Q. Lu, Y. Yu, H. Xu, Y. Zhao, H. Zhang, *Adv. Mater.* 27 (2015) 7372–7378.
- [85] Y. Wang, M. Zhao, J. Ping, B. Chen, X. Cao, Y. Huang, C. Tan, Q. Ma, S. Wu, Y. Yu, Q. Lu, J. Chen, W. Zhao, Y. Ying, H. Zhang, *Adv. Mater.* 28 (2016) 4149–4155.
- [86] M. Tian, F. Pei, M. Yao, Z. Fu, L. Lin, G. Wu, G. Xu, H. Kitagawa, X. Fang, *Energy Storage Mater.* (2018), <https://doi.org/10.1016/j.ensm.2018.12.016>.
- [87] R. Koitz, M. Iannuzzi, J. Hutter, *J. Phys. Chem. C* 119 (2015) 4023–4030.
- [88] H. Spillmann, A. Dmitriev, N. Lin, P. Messina, J.V. Barth, K. Kern, *J. Am. Chem. Soc.* 125 (2003) 10725–10728.
- [89] S. Stepanow, M. Lingenfelder, A. Dmitriev, H. Spillmann, E. Delvigne, N. Lin, X. Deng, C. Cai, J.V. Barth, K. Kern, *Nat. Mater.* 3 (2004) 229–233.
- [90] S. Clair, S. Pons, H. Brune, K. Kern, J.V. Barth, *Angew. Chem., Int. Ed.* 44 (2005) 7294–7297.
- [91] A.P. Seitsonen, M. Lingenfelder, H. Spillmann, A. Dmitriev, S. Stepanow, N. Lin, K. Kern, J.V. Barth, *J. Am. Chem. Soc.* 128 (2006) 5634–5635.
- [92] S. Stepanow, N. Lin, D. Payer, U. Schlickum, F. Kappenberger, G. Zoppellaro, M. Ruben, H. Brune, J.V. Barth, K. Kern, *Angew. Chem., Int. Ed.* 46 (2007) 710–713.
- [93] S. Fabris, S. Stepanow, N. Lin, P. Gambardella, A. Dmitriev, J. Honolka, S. Baroni, K. Kern, *Nano Lett.* 11 (2011) 5414–5420.
- [94] A. Langner, S.L. Tait, N. Lin, R. Chandrasekar, V. Meded, K. Fink, M. Ruben, K. Kern, *Angew. Chem., Int. Ed.* 51 (2012) 4327–4331.
- [95] Y. Li, J. Xiao, T.E. Shubina, M. Chen, Z. Shi, M. Schmid, H.P. Steinruck, J.M. Gottfried, N. Lin, *J. Am. Chem. Soc.* 134 (2012) 6401–6408.
- [96] A. Dmitriev, H. Spillmann, N. Lin, J.V. Barth, K. Kern, *Angew. Chem., Int. Ed.* 42 (2003) 2670–2673.
- [97] K. Töllner, R.P. Biro, M. Lahav, D. Milstein, *Science* 278 (1997) 2100–2102.
- [98] D.Y. Takamoto, E. Aydil, J.A. Zasadzinski, A.T. Ivanova, D.K. Schwartz, T. Yang, P.S. Cremer, *Science* 293 (2001) 1292–1295.
- [99] D.J. Qian, C. Nakamura, J. Miyake, *Langmuir* 16 (2000) 9615–9619.
- [100] D.J. Qian, C. Nakamura, J. Miyake, *Chem. Commun.* (2001) 2312–2313.
- [101] C. Scherb, A. Schödel, T. Bein, *Angew. Chem. Int. Ed.* 57 (2008) 5777–5779.
- [102] O. Shekhah, H. Wang, S. Kowarik, F. Schreiber, M. Paulus, M. Tolan, C. Sternemann, F. Evers, D. Zacher, R.A. Fischer, C. Wöll, *J. Am. Chem. Soc.* 129 (2007) 15118–15119.
- [103] O. Shekhah, H. Wang, M. Paradinas, C. Wöll, *Nature Mater.* 8 (2009) 481–484.
- [104] R. Makiura, S. Motoyama, Y. Umemura, H. Yamanaka, O. Sakata, H. Kitagawa, *Nature Mater.* 9 (2010) 565–571.
- [105] T. Bauer, Z. Zheng, A. Renn, R. Enning, A. Stemmer, J. Sakamoto, A.D. Schlüter, *Angew. Chem. Int. Ed.* 50 (2011) 7879–7884.
- [106] R. Makiura, R. Usui, Y. Sakai, A. Nomoto, A. Ogawa, O. Sakata, A. Fujiwara, *ChemPlusChem* 79 (2014) 1352–1360.
- [107] R. Makiura, K. Tsuchiyama, O. Sakata, *CrystEngComm* 13 (2011) 5538–5541.
- [108] R. Makiura, O. Kononov, *Dalton Trans.* 42 (2013) 15931–15936.
- [109] Z. Zheng, L. Opilik, F. Schiffmann, W. Liu, G. Bergamini, P. Ceroni, L.T. Lee, A. Schütz, J. Sakamoto, R. Zenobi, J. VandeVondele, A.D. Schlüter, *J. Am. Chem. Soc.* 136 (2014) 6103–6110.
- [110] R. Makiura, O. Kononov, *Sci. Rep.* 3 (2013) 2506–2514.
- [111] Z. Zheng, C.S. Ruiz-Vargas, T. Bauer, A. Rossi, P. Payammar, A. Schütz, A. Stemmer, J. Sakamoto, A.D. Schlüter, *Macromol. Rapid Commun.* 34 (2013) 1670–1680.
- [112] Y. Cheng, X. Wang, C. Jia, Y. Wang, L. Zhai, Q. Wang, D. Zhao, *J. Membr. Sci.* 539 (2017) 213–223.
- [113] Y. Yang, K. Goh, R. Wang, T.H. Bae, *Chem. Commun.* 53 (2017) 4254–4257.
- [114] Z. Kang, Y. Peng, Z. Hu, Y. Qian, C. Chi, L.Y. Ye, L. Tee, D. Zhao, *J. Mater. Chem. A* 3 (2015) 20801–20810.
- [115] X. Wang, C. Chi, K. Zhang, Y. Qian, K.M. Gupta, Z. Kang, J. Jiang, D. Zhao, *Nat. Commun.* 8 (2017) 14460.
- [116] R. Dong, Z. Zheng, D.C. Tranca, J. Zhang, N. Chandrasekhar, S. Liu, X. Zhuang, G. Seifert, X. Feng, *Chem-Eur. J.* 23 (2017) 2255–2260.
- [117] J. Duan, S. Chen, C. Zhao, *Nat Commun.* 8 (2017) 15341.
- [118] Z. Hu, E.M. Mahdi, Y. Peng, Y. Qian, B. Zhang, N. Yan, D. Yuan, J.C. Tan, D. Zhao, *J. Mater. Chem. A* 5 (2017) 8954–8963.
- [119] Z. Lin, N.C. Thacker, T. Sawano, T. Drake, P. Ji, G. Lan, L. Cao, S. Liu, C. Wang, W. Lin, *Chem. Sci.* 9 (2018) 143–151.
- [120] Z. Zhang, Y. Chen, S. He, J. Zhang, X. Xu, Y. Yang, F. Nosheen, F. Saleem, W. He, X. Wang, *Angew. Chem. Int. Ed.* 53 (2014) 12517–12521.
- [121] S. He, Y. Chen, Z. Zhang, B. Ni, W. He, X. Wang, *Chem. Sci.* 7 (2016) 7101–7105.
- [122] Y. Huang, M. Zhao, S. Han, Z. Lai, J. Yang, C. Tan, Q. Ma, Q. Lu, J. Chen, X. Zhang, Z. Zhang, B. Li, B. Chen, Y. Zong, H. Zhang, *Adv. Mater.* 29 (2017) 1700102.
- [123] W.J. Song, *Talanta* 170 (2017) 74–80.
- [124] Z.Q. Li, L.G. Qiu, W. Wang, T. Xu, Y. Wu, X. Jiang, *Inorg. Chem. Commun.* 11 (2008) 1375–1377.
- [125] A.K. Chaudhari, H.J. Kim, I. Han, J.C. Tan, *Adv. Mater.* 29 (2017) 1701463.
- [126] M. Tian, Z.H. Fu, B. Nath, M.S. Yao, *RSC Adv.* 6 (2016) 88991–88995.
- [127] F. Su, S. Zhang, H. Ji, H. Zhao, J.Y. Tian, C.S. Liu, Z. Zhang, S. Fang, X. Zhu, M. Du, *ACS Sensor* 2 (2017) 998–1005.
- [128] F. Cao, M. Zhao, Y. Yu, B. Chen, Y. Huang, J. Yang, X. Cao, Q. Lu, X. Zhang, Z. Zhang, C. Tan, H. Zhang, *J. Am. Chem. Soc.* 138 (2016) 6924–6927.
- [129] Q. Lu, M. Zhao, J. Chen, B. Chen, C. Tan, X. Zhang, Y. Huang, J. Yang, F. Cao, Y. Yu, J. Ping, Z. Zhang, X.J. Wu, H. Zhang, *Small* 12 (2016) 4669–4674.
- [130] L. Cao, Z. Lin, W. Shi, Z. Wang, C. Zhang, X. Hu, C. Wang, W. Lin, *J. Am. Chem. Soc.* 139 (2017) 7020–7029.
- [131] M. Xu, S. Yuan, X.Y. Chen, Y.J. Chang, G. Day, Z.Y. Gu, H.C. Zhou, *J. Am. Chem. Soc.* 139 (2017) 8312–8319.
- [132] W. Shi, L. Cao, H. Zhang, X. Zhou, B. An, Z. Lin, R. Dai, J. Li, C. Wang, W. Lin, *Angew. Chem. Int. Ed.* 56 (2017) 9704–9709.